Journal of Applied Fluid Mechanics, Vol. 17, No. 2, pp. 497-518, 2024.
Available online at www.jafmonline.net, ISSN 1735-3572, EISSN 1735-3645.
https://doi.org/10.47176/jafm.17.02.2011

Numerical Study on Effect of High-rise Building on Wind and Thermal Environments in Idealized Urban Array: Impacts of Planar Density

P. Ding[1,2†] and X. Zhou[2]

[1] *Guangzhou Panyu Polytechnic, Guangzhou, Guangdong, 511483, China*
[2] *School of Civil Engineering, Guangzhou University, Guangzhou, Guangdong, 510006, China*

†*Corresponding Author Email: dingpx@gzpyp.edu.cn, tingalan@foxmail.com*

ABSTRACT

How the high-rise (HR) building affects the pedestrian-level wind environment (PLWE) is of great significance to urban planning. Therefore, the effects of the HR building on the wind and the thermal environments in the urban array with different planar densities are studied numerically. The planar densities are 0.25, 0.4 and 0.6. The simulation results reveal that the HR building can strongly affect the flow dynamics and the heat transfer mechanisms in the urban array. Compared with the low-rise (LR) buildings, the presence of the HR building in the surrounding buildings creates high-speed downwash airflow in the upstream street, and the velocity of downwash airflow increases with the increase of planar density. The turbulent kinetic energy at pedestrian level around the HR building increases. When the planar density is large, the direction of the wake airflow behind the HR building is alternating. And long periods of high-speed airflow are observed, which do not occur in the wake of the target LR building. The temperature around the HR building is lower than that around the target LR building. The surface heat flux around the HR building is greater than that around the target LR building. The surface heat flux around the HR building increases with the increase of the planar density, which is contrary to that around the target LR building.

Article History

Received May 15, 2023
Revised September 28, 2023
Accepted October 5, 2023
Available online December 4, 2023

Keywords:

Numerical simulation
Wind
Thermal environment
High-rise building
Urban array
Planar density

1. INTRODUCTION

The strong downwash around the high-rise (HR) building amplifies the wind speed at ground layer. This will often cause an uncomfortable or dangerous wind environment for urban pedestrians. Therefore, how the HR building affects the pedestrian-level wind environment (PLWE) is an important topic (Blocken et al., 2016; Mittal et al., 2018). Through boundary layer wind tunnel experiment (WTE), numerical simulation and other methods, a large amount of basic research has been carried out to control or reduce pedestrian wind speed (Stathopoulos, 1985; Uematsu et al., 1992; Tsang et al., 2012; Kuo et al., 2015; Tamura et al., 2017; Tse et al., 2017; Xia et al., 2017; Zhang et al., 2017; Mittal et al., 2019; Tamura et al., 2019; Van Druenen et al., 2019).

Geometric modification is an important strategy to control the PLWE around HR buildings and includes addition of podiums (Tsang et al., 2012; Kuo et al., 2015; Van Druenen et al., 2019), corner modifications (Stathopoulos, 1985; Uematsu et al., 1992; Mittal et al., 2019; Tamura et al., 2017), varying building sizes (Tsang et al., 2012) and lift-up designs (Tse et al., 2017; Xia et al., 2017; Zhang et al., 2017). The approaching flow is an important factor too (Tsang et al., 2012; Tamura et al., 2019). The WTE of Ref. (Tamura et al., 2017) shows that corner-chamfering and corner-cutting can reduce areas of high wind speed around HR buildings by up to 30%.

In practice, a complex flow interaction is caused by the HR building and its surrounding buildings. However, it is difficult to study this complex interaction in an actual urban configuration systematically. This is because there is a large number of geometric combinations between the target building and the surrounding buildings, and the results vary with the combinations (Tominaga & Shirzadi, 2021). Therefore, the urban layout was simplified down to an array of buildings, to highlight the main effects.

Tsang et al. conducted experiments for providing a basic study on the interaction between wind and structure (Tsang et al., 2012). This experimental study focusses on

NOMENCLATURE

a	width of the cubic buildings	T_H	temperature of the inlet at the height of the high-rise isolated building
b	width of the high-rise isolated building	u_h	wind speed at surrounding buildings` height
C_μ	model constant	u_H	wind speed at the high-rise isolated building`s height
F_1, F_2	shielding function	V	cell volume
g	gravity	x, y, z	coordinate axis
h	height of the surrounding buildings	ΔT	|TH-Tf |/[K]
H	height of the high-rise isolated building	δ_{ij}	Kronecker delta
h_{max}	maximum edge length of the cell	ε	turbulence dissipation rate
p	pressure	μ	viscosity
P_k	generation of turbulence kinetic energy	μ_{sgs}	subgrid scale eddy viscosity
Pr	Prandtl number = 0.71	μ_t	turbulent viscosity
s	distance between two buildings	ν	kinematic viscosity
S	modulus of the mean rate of strain tensor	ρ	density
S_{ij}	strain rate tensor	τ_{ij}	Reynolds stress
T	temperature	ω	specific dissipation rate
T_b	temperature of the building wall	$\overline{\quad}$	ensemble averaged
T_f	temperature of the ground surface	i,j	vector

the impact of building size and separation, rows of buildings and podium on PLWE. The results show that a single wider building adversely affects the natural ventilation at pedestrian level, while a high building improves the near-field ventilation. When the building separation is less than half of the building width, the natural ventilation at pedestrian level is adversely affected. The addition of a podium also adversely affects the airflow around the building.

The characteristics of the PLWE in the street canyon under different street widths, podium heights and approaching wind directions were determined through the WTE conducted by Kuo et al. (Kuo et al., 2015). The experimental results show that the effect of street canyon width on the PLWE can be divided into three different flow modes. In the street canyon, the higher podium creates stronger wind speeds, and the different approaching wind directions change the high-speed areas.

The influence of wind incident angle and passage width on wind characteristics at the re-entrant corners of cross-shaped HR buildings is investigated by Iqbal and Chan (Iqbal & Chan, 2016) and the effects of the stagnation zone and wake zone on the ventilation and wind comfort under different wind incident directions were also studied.

Tominaga and Shirzadi used the WTE to measure the wind speed around an urban block model composed of low-rise (LR) buildings with an HR building in the center (Tominaga & Shirzadi, 2021). The presence of the HR building greatly alters the airflow characteristics of the PLWE around the building, because of the complex interaction between the HR building and its surrounding street canyons. The HR building produces large velocity fluctuations compared with the LR building. Furthermore, Shirzadi and Tominaga proposed a multi-fidelity shape optimization framework for improving the PLWE (Shirzadi & Tominaga, 2021).

Additionally, outdoor thermal comfort is also an important factor for designing buildings and urban planning. The investigations of the thermal field are mainly focused on the urban array where the heights of the buildings are the same. The purpose of the study of Du and his co-authors is to determine the optimal PLEW and outdoor thermal comfort configuration in an ideal urban canyon where each building has a lift-up design (Du et al., 2019). The final optimal design scheme of the ideal urban canyon is obtained.

A large eddy simulation (LES) was used to analyze the mean flow and turbulence in a regular building array at different Richardson number by Duan and Ngan (Duan & Ngan, 2019). The skimming flow persists for stable and neutral conditions. However, under unstable conditions, updraft dominates.

The effect of thermal stability on the ventilation of a cubic buildings array was also studied by Duan and Ngan (Duan & Ngan, 2020). The effect of atmospheric stratification on the airflow and the concentration around a rectangular building array with the regular arrangement is studied through WTE conducted by Marucci and Carpentieri (Marucci & Carpentieri, 2020). The effects of surface heating conditions and aspect ratios on the flow and temperature fields in the WTE were investigated using particle image velocimetry (Lin et al., 2020).

Limitations of these studies, which are summarized in Table 1, about the complex interaction between the HR building and its surrounding buildings are the facts that only one planar density is considered and the thermal environment influenced by the HR building is ignored. Therefore, the impact of planar density on wind and thermal environment in an idealized urban array with and

Table 1 Summary of literatures

Literatures	Method	Building model	Content
Tsang et al. (2012)	WTE	Isolated HR building	Wind environment
Kuo et al. (2015)	WTE	Isolated HR building	Wind environment
Iqbal and Chan (2016)	Numerical simulation	Array of HR buildings	Wind environment
Van Druenen et al. (2019)	Numerical simulation	Isolated HR building	Wind environment
Stathopoulos (1985)	WTE	Isolated HR building	Wind environment
Uematsu et al. (1992)	Numerical simulation	Isolated HR building	Wind environment
Tamura et al. (2017)	Numerical simulation	Isolated HR building	Wind environment
Mittal et al. (2019)	Numerical simulation	Isolated HR building	Wind environment
Zhang et al. (2017)	WTE	Isolated HR building	Wind environment
Xia et al. (2017)	Numerical simulation	Isolated HR building	Wind environment
Tse et al. (2017)	WTE	Isolated HR building	Wind environment
Tamura et al. (2019)	WTE	Isolated HR building	Wind environment
Tominaga and Shirzadi (2021)	WTE	Building array with HR building	Wind environment
Shirzadi and Tominaga (2021)	Numerical simulation	Isolated HR building	Wind environment
Du et al. (2019)	Numerical simulation	Building array	Wind and thermal environment
Duan and Ngan (2019)	Numerical simulation	Building array	Wind and thermal environment
Duan and Ngan (2020)	Numerical simulation	Building array	Wind and thermal environment
Marucci and Carpentieri (2020)	WTE	Building array	Wind and thermal environment
Lin et al. (2020)	WTE	Building array	Wind and thermal environment
Yoshie (2016)	WTE & Numerical simulation	Isolated HR building	Wind and thermal environment

without an HR building is studied numerically. How the high-rise building affects the flow dynamics and the heat transfer mechanisms in the urban array is studied. A zonal RANS/LES method is used in this study.

2. DESCRIPTION OF STUDY CASES

For analyzing the effect of HR buildings on the wind and the thermal environments in an urban array under varying planar density, the WTE conducted by Tominaga and Shirzadi (2021) is chosen as the reference case. The geometry and the top view with position indicators are displayed in Fig. 1. The ranges of the x, y and z directions are respectively (-7.5h, 20h), (-7.5h, 7.5h), (0, 18h), where h = 0.1 m is the height of the surrounding buildings. The HR building (target building) with a height having the value of 0.3 m is located at (x, y, z) = (0, 0, 0) and is sheltered by eight cubic buildings. The width of the cubic buildings a = 0.1 m. The distance between two buildings in the sheltered condition is s = 0.2m, which means that the planar area density is 0.25. The wind speed at surrounding buildings` height was measured to be u_h = 3.1 m/s, yielding Reynolds number of about 21 000. For studying the effect of the planar density, the distances between the two buildings' centers are 130 mm, 158 mm and 200 mm, leading to the planar densities (PDs) having the values of 0.6, 0.4 and 0.25.

Additionally, the results of the unstable non-isothermal WTE conducted by Yoshie (2016) are chosen to validate the performance of the used numerical approach in predicting unstable non-isothermal airflow around an isolated building. The geometry is displayed in Fig. 2. The ranges of the x, y and z directions are respectively (-3H, 7.5H), (-3.125H, 3.125H), (0, 5.625H), where H = 0.16 m is the height of the HR isolated building. The HR isolated building is located at (x, y, z) = (-0.25H, 0, 0). The width of the quadrate cross-section b = 0.08 m. The wind speed at the building`s height was measured to be u_H = 1.37 m/s, yielding a Reynolds number of about 15 000.

3. NUMERICAL METHODS

3.1 Equations

Air is considered here as an ideal gas when temperature of air changes. The continuity, momentum and temperature equations are as follows.

$$\frac{\partial \rho}{\partial t}+\frac{\partial}{\partial x_i}\left(\rho \overline{u_i}\right) \tag{1}$$

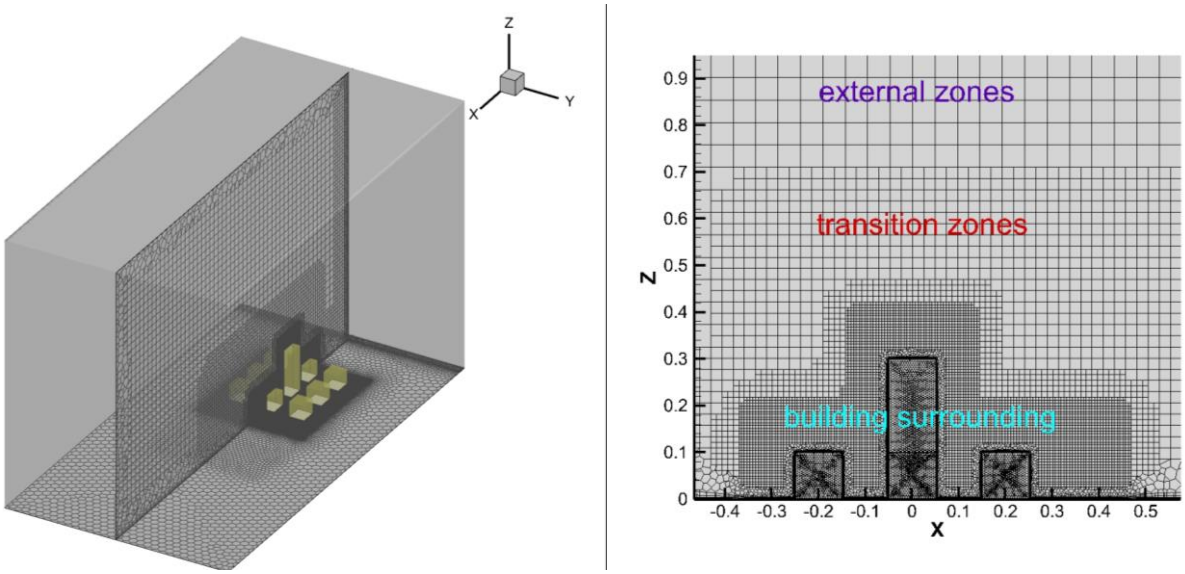

(a) geometry with grid (b) grid partitioning

(c) top view with position indicators

Fig. 1 Computational domain of the urban array

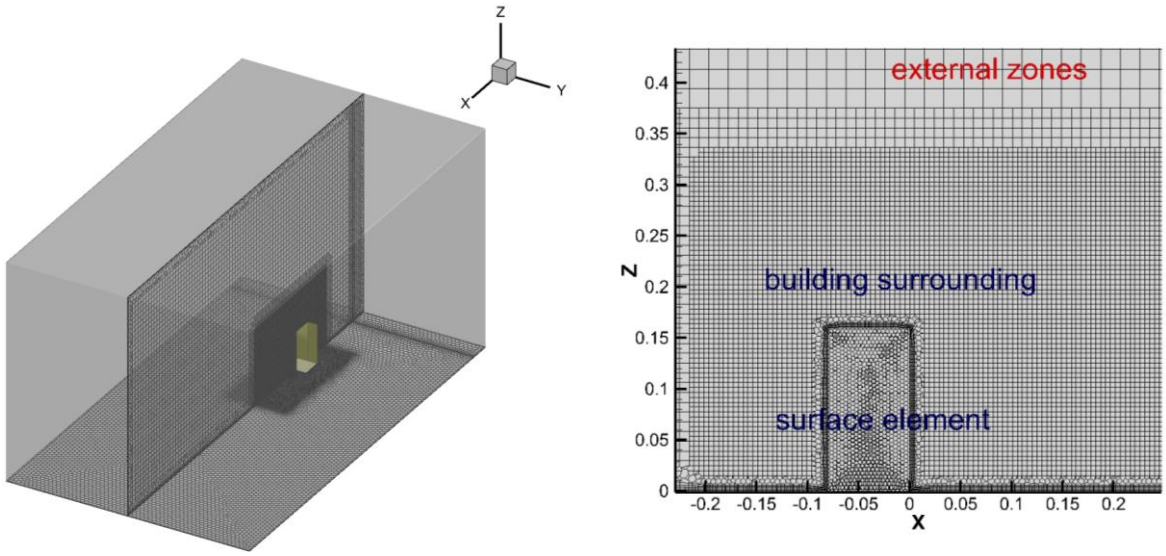

(a) geometry with grid (b) grid partitioning

Fig. 2 Computational domain of the isolated HR building

$$\frac{\partial}{\partial t}\left(\rho\overline{u_i}\right)+\frac{\partial}{\partial x_j}\left(\rho\overline{u_i}\overline{u_j}\right)=-\frac{\partial\overline{p}}{\partial x_i}+ \tag{2}$$
$$\frac{\partial}{\partial x_j}\left[\mu\left(\frac{\partial\overline{u_i}}{\partial x_j}+\frac{\partial\overline{u_j}}{\partial x_j}-\frac{2}{3}\delta_{ij}\frac{\partial\overline{u_l}}{\partial x_l}\right)\right]+\frac{\partial\tau_{ij}}{\partial x_j}+\rho\delta_{i3}g$$

$$\frac{\partial}{\partial t}\left(\rho\overline{T}\right)+\frac{\partial}{\partial x_i}\left(\rho u_i\overline{T}\right)=\frac{\partial}{\partial x_i}\left[\left(\frac{\mu}{Pr}+\frac{\mu_t}{Pr_t}\right)\frac{\partial\overline{T}}{\partial x_i}\right] \tag{3}$$

where the symbols are explained in Nomenclature.

The SST k-ω model (Menter, 1994) is chosen as the underlying RANS model of the zonal RANS/LES method. The turbulence kinetic energy k and the specific dissipation rate ω in the zonal RANS/LES method are as follows.

$$\frac{\partial}{\partial t}\left(\rho k\right)+\frac{\partial}{\partial x_i}\left(\rho\overline{u_i}k\right)=P_k-\rho\beta^*k\omega+\frac{\partial}{\partial x_i}\left[\left(\mu+\frac{\mu_t}{\sigma_k}\right)\frac{\partial k}{\partial x_i}\right] \tag{4}$$

$$\frac{\partial}{\partial t}\left(\rho\omega\right)+\frac{\partial}{\partial x_i}\left(\rho\overline{u_i}\omega\right)=\alpha\frac{\omega}{k}P_k-\rho\beta\omega^2+ \tag{5}$$
$$\frac{\partial}{\partial x_i}\left[\left(\mu+\frac{\mu_t}{\sigma_\omega}\right)\frac{\partial\omega}{\partial x_i}\right]+2(1-F_1)\frac{\rho}{\sigma_{\omega2}\omega}\frac{\partial k}{\partial x_i}\frac{\partial\omega}{\partial x_i}$$

The production term P_k is calculated below.

$$P_k=\mu_tS^2,\quad S=\sqrt{2S_{ij}S_{ij}} \tag{6}$$
$$S_{ij}=0.5\left(\partial\overline{u_i}/\partial x_j+\partial\overline{u_j}/\partial x_i\right)$$

The turbulent viscosity in the RANS zone is

$$\mu_{tRANS}=\rho\frac{k}{\omega}\frac{1}{\max\left[1/\alpha,SF_2/(0.31\omega)\right]} \tag{7}$$

The turbulent viscosity in the LES zone uses the WALE turbulent viscosity (Nicoud & Ducros, 1999), and its formula is as follows.

$$\mu_{sgs}=\rho L_s^2\frac{\left(S_{ij}^dS_{ij}^d\right)^{3/2}}{\left(S_{ij}S_{ij}\right)^{5/2}+\left(S_{ij}^dS_{ij}^d\right)^{5/4}} \tag{8}$$

$$L_s=0.325V^{1/3} \tag{9}$$

$$S_{ij}^d=0.5(g_{ij}^2+g_{ji}^2)-(1/3)\delta_{ij}g_{kk}^2,g_{ij}=\partial\overline{u_i}/\partial x_j \tag{10}$$

The turbulent viscosity is calculated as follows.

$$\mu_t=\mathrm{MIN}\left(\mu_{sgs},\mu_{tRANS}\right) \tag{11}$$

In this hybrid RANS/LES method, when μ_{tRANS} is less than μ_{sgs}, which occurs near walls, the RANS model works. Otherwise, μ_{tRANS} is larger than μ_{sgs} away from walls, then the LES mode works. This methodology is similar to other hybrid RANS/LES models including DES (Spalart, 2009) and PLES (Ding & Zhou, 2022; Ding et al., 2022) models.

3.2 Boundary Conditions and Grids

The inlet boundary conditions are the same as the WTEs (Tominaga & Shirzadi, 2021; Yoshie, 2016) in the test cases, which are displayed in Fig. 3. The turbulence

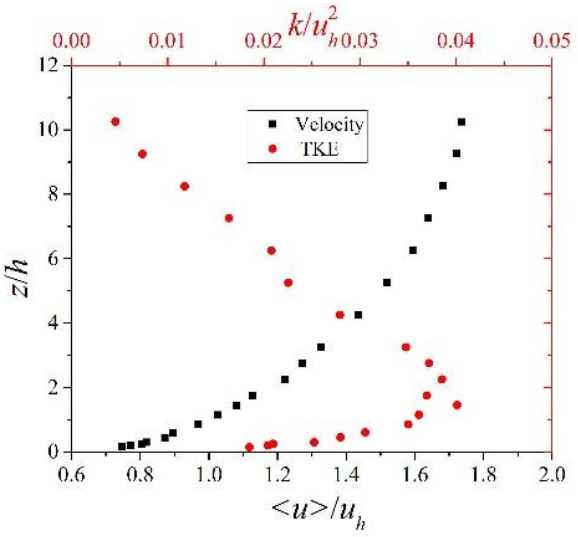

(a) urban array

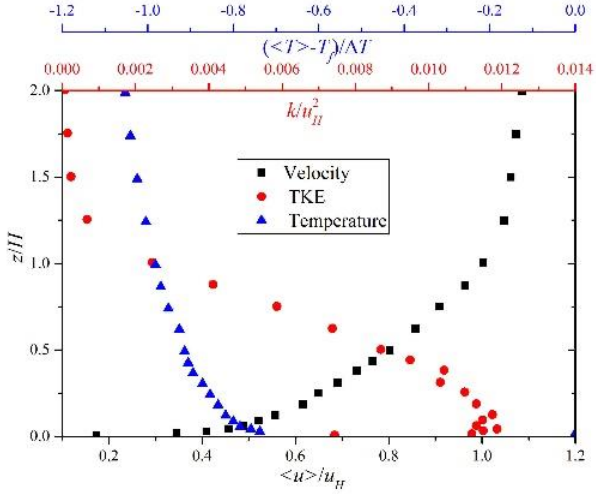

(b) isolated HR building

Fig. 3 Inlet boundary condition for the urban array (a) and the isolated HR building (b) test cases

dissipation rate ε and the specific dissipation rate ω are given by

$$\varepsilon=C_\mu^{1/2}k\frac{du}{dz} \tag{13}$$

$$\omega=\frac{\varepsilon}{C_\mu k}=\frac{\varepsilon}{0.09k} \tag{14}$$

The building and ground surfaces are set to the wall boundary condition. The lateral and upper walls of the computational domain are regarded as the symmetry boundary. The pressure-out boundary condition is used at the outlet. The random 2D vortices are generated by the vortex method (Mathey et al., 2006) away from the inlet, at h and $0.5H$ for the urban array and the isolated HR building cases respectively. This setting speeds up the convergence, which is proven in our previous paper (Ding et al., 2022). For the isolated HR building case, the temperature of the ground surface is T_f = 318.45 K, and the temperature of the building wall is T_b = 314.85 K. The temperature of the inlet at the height of the HR isolated building is T_H = 284.45 K, and the absolute value of

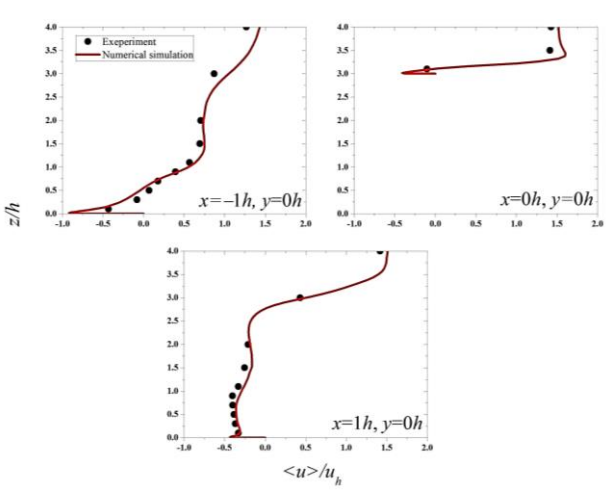

(a) y/h=0 streamwise velocity

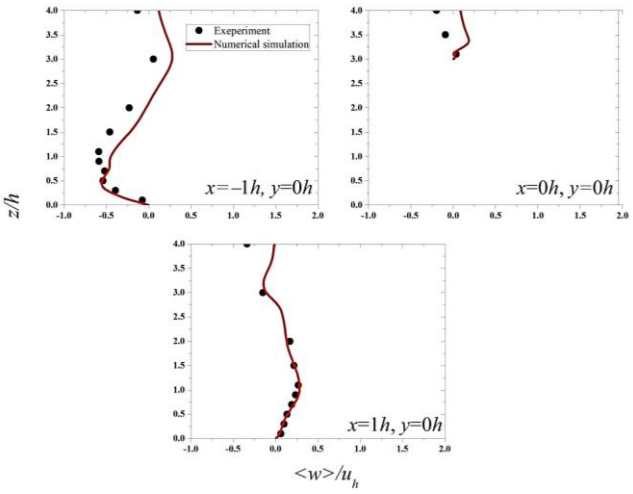

(b) y/h=0 vertical velocity

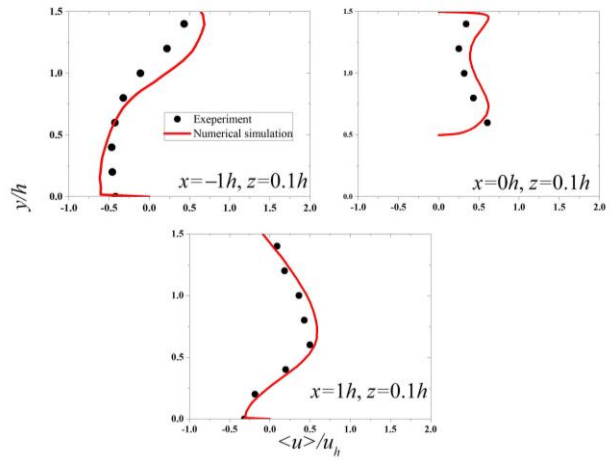

(c) z/h = 0.1 streamwise velocity

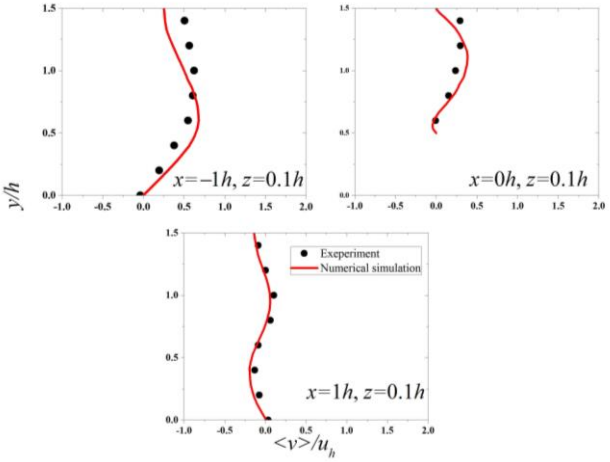

(d) z/h = 0.1 horizontal velocity

Fig. 4 Comparison of the mean velocity on planes y/h=0 (a)(b) and z/h = 0.1 (c)(d) from the numerical simulation with the experimental result (Tominaga & Shirzadi, 2021) for the isothermal urban array test cases

temperature difference, $\Delta T=|T_H - T_f|=$ 34.00 K. The temperature boundary condition of the urban array study case is the same as the isolated HR building test case, except for the inlet where the temperature is uniform. The temperature at the inlet is 284.45K. The flow conditions are the same as the urban array test cases, so the Reynolds number is 21 000. This means that the inlet condition is isothermal. In this simulation, the solver uses the ideal gas law to compute the density.

The grid outlines are shown in Figs. 1 and 2. The first cell rows near the building and the ground surfaces are refined to keep the y plus below 5.0. For the urban array cases, the basic size of the surface element over the building wall is 0.005 m, and the sizes of volume elements in the building surroundings, the transition, and the external zones are 0.006 m, 0.024 m, and 0.048 m, respectively. For the finer grid, the size of the surface element over the building wall is 0.004 m, and the sizes of volume elements in the building surrounding, the transition and the external zones are 0.005 m, 0.018 m and 0.036 m respectively. The basic number of cells is about 1.7 million. A finer grid with about 3.3 million cells is used for the grid-independent study. Taking the results from the finer grid as the reference data, the *NMSE* (normalized mean square error) value of the basic grid is 0.0012. Therefore, the basic grid replicates well the grid independence result. For the isolated HR building case, the grid resolution used is the same as in our simulation study in Ding et al. (2022).

The numerical method is the same as in our previous paper (Ding et al., 2022). The code used is ANSYS FLUENT. The SIMPLEC algorithm is used for the pressure-velocity coupling. The Bounded Central Differencing scheme and the second-order upwind scheme are used to discretize the momentum equation and the SST k-ω equations, respectively. The time step and statistical time are set to 5.0×10^{-4} s and 30.0 s, respectively. The statistic begins at 8.0 s, which can remove the influence of the initialization. The convergent residuals of the continuity, the momentum, the temperature and the turbulence equations are set to $1.0e^{-5}$, $1.0e^{-6}$, $1.0e^{-8}$ and $1.0e^{-6}$, respectively.

4. RESULTS AND DISCUSSION

4.1 Validation of the Numerical Approach

The comparisons of the mean (time-averaged) velocity and the turbulence kinetic energy (TKE) from the numerical simulation with the experimental result (Tominaga & Shirzadi, 2021) for the isothermal urban array test case are presented in Figs. 4 and 5 respectively.

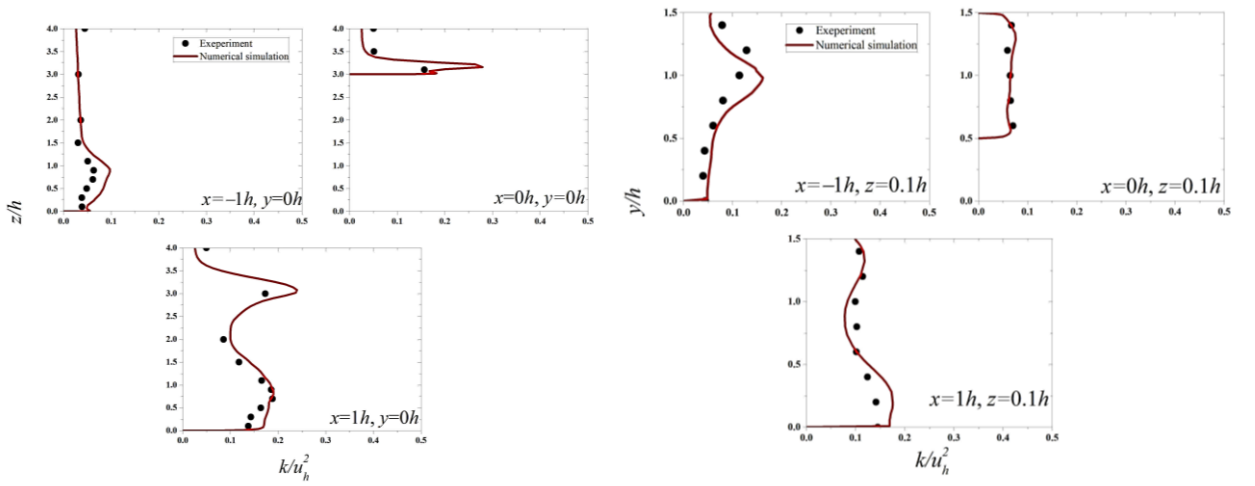

(a) y/h=0 (b) z/h = 0.1

Fig. 5 Comparison of TKE on the planes y/h=0 (a) and z/h = 0.1(b) from the numerical simulation with the experimental result for the isothermal urban array test case

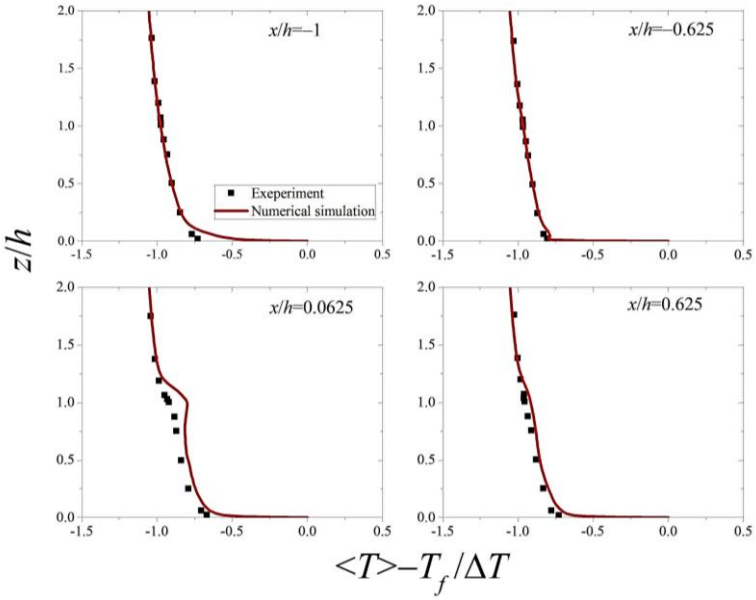

Fig. 6 Comparison of mean temperature on the plane y/h=0 from the numerical simulation with the experimental result for the isolated non-isothermal HR building test case

Figure 4 proves that the predicted mean velocity conforms well to the experimental data. The TKE is predicted worse than the velocity, which is shown in Fig. 5. This phenomenon is also found in many resolved scale simulations (Gousseau et al., 2013; Ding et al., 2022).

The comparisons of the mean temperature and mean streamwise velocity from the numerical simulation with the experimental data (Yoshie, 2016) for the isolated non-isothermal HR building test case are presented in Figs. 6 and 7 respectively. Figure 6 proves that the predicted mean temperature conforms well to the experimental data, except on the line (x/H= 0.625, y/H=0). The obtained mean streamwise velocity is slightly under-predicted, which also exists in the LES computation (Bazdidi-Tehrani et al., 2019).

The above test cases prove that the numerical method used could not give perfect agreement, but it highlights the features of the non-isothermal flow and the thermal field around buildings or urban arrays. Next, the effect of an HR building on the wind and thermal environment in an urban array with different planar densities is investigated using the used numerical method.

4.2 Flow Field

The mean streamlines on the plane y/h=0 for the urban array cases is shown in Fig. 8. Obviously, due to the HR building, the flow structures around the target buildings which are located at the center of the urban array differ significantly. Fig. 8(a-1, a-2, a-3) display that the air flows to the HR building, then flows down to the upstream street canyon. Another partial airflow is directed upward and

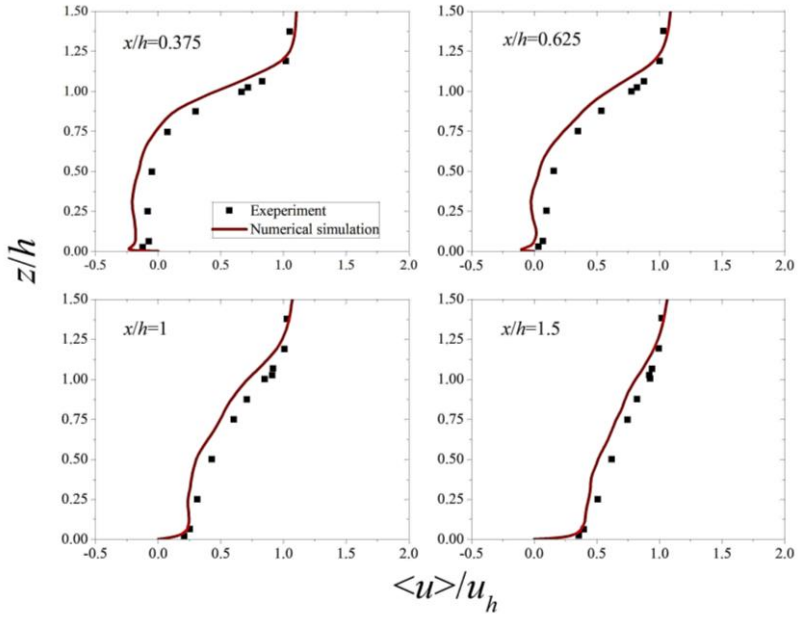

Fig. 7 Comparison of mean streamwise velocity on the plane *y*/*H*=0 from the numerical simulation with the experimental result for the isolated non-isothermal HR building test case

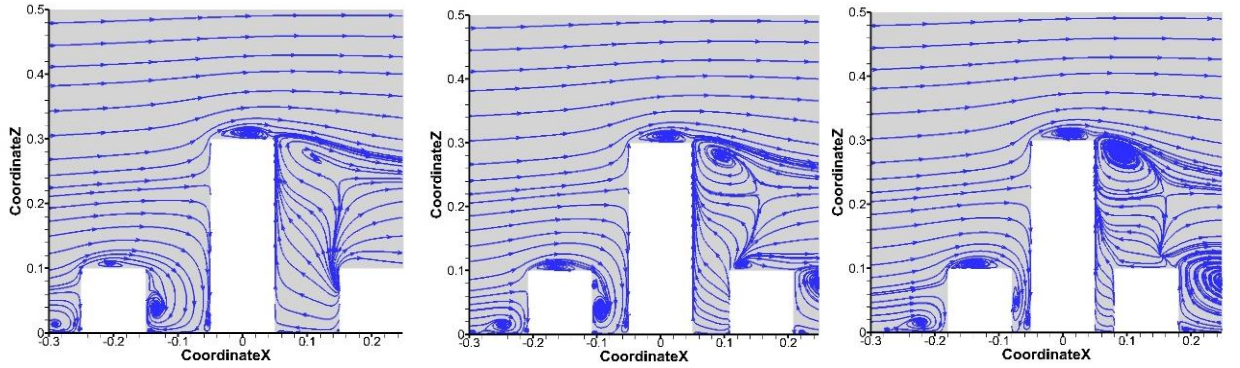

(a-1) HR building PD = 0.25 (a-2) HR building PD = 0.4 (a-3) HR building PD = 0.6

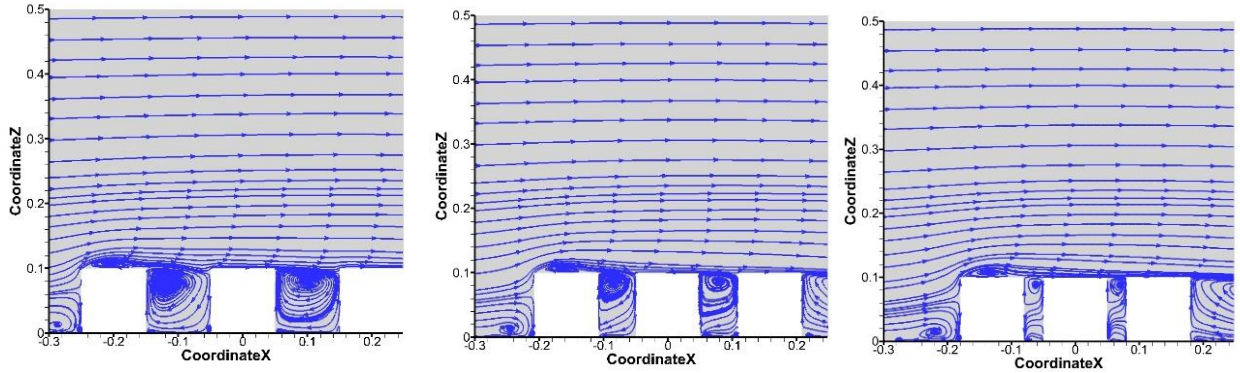

(b-1) LR building PD = 0.25 (b-2) LR building PD = 0.4 (b-3) LR building PD = 0.6

Fig. 8 Mean streamlines on the plane *y*/*h*=0 for the urban array cases. a: HR building, b: LR building

separates at the roof corner. On the contrary, for the LR building, only the downward airflow appears in front of the surrounded LR building. And there is no separating airflow over the roof, which is displayed in Fig. 8(b-1, b-2, b-3). It is noted that the airflow structures in front of and behind the target LR building, where two vortices form, are similar. The two vortices become smaller for the higher density array. Due to the HR building, airflow structures in front of and behind it are very different. More than two vortices form in front of the HR building, but in the street, there is no vortex appearing behind it. The Q-criteria=30000 for the urban array cases is shown in Fig. 9. It is observed that lots of vortices form around the target HR buildings, while there is much less vortex activity

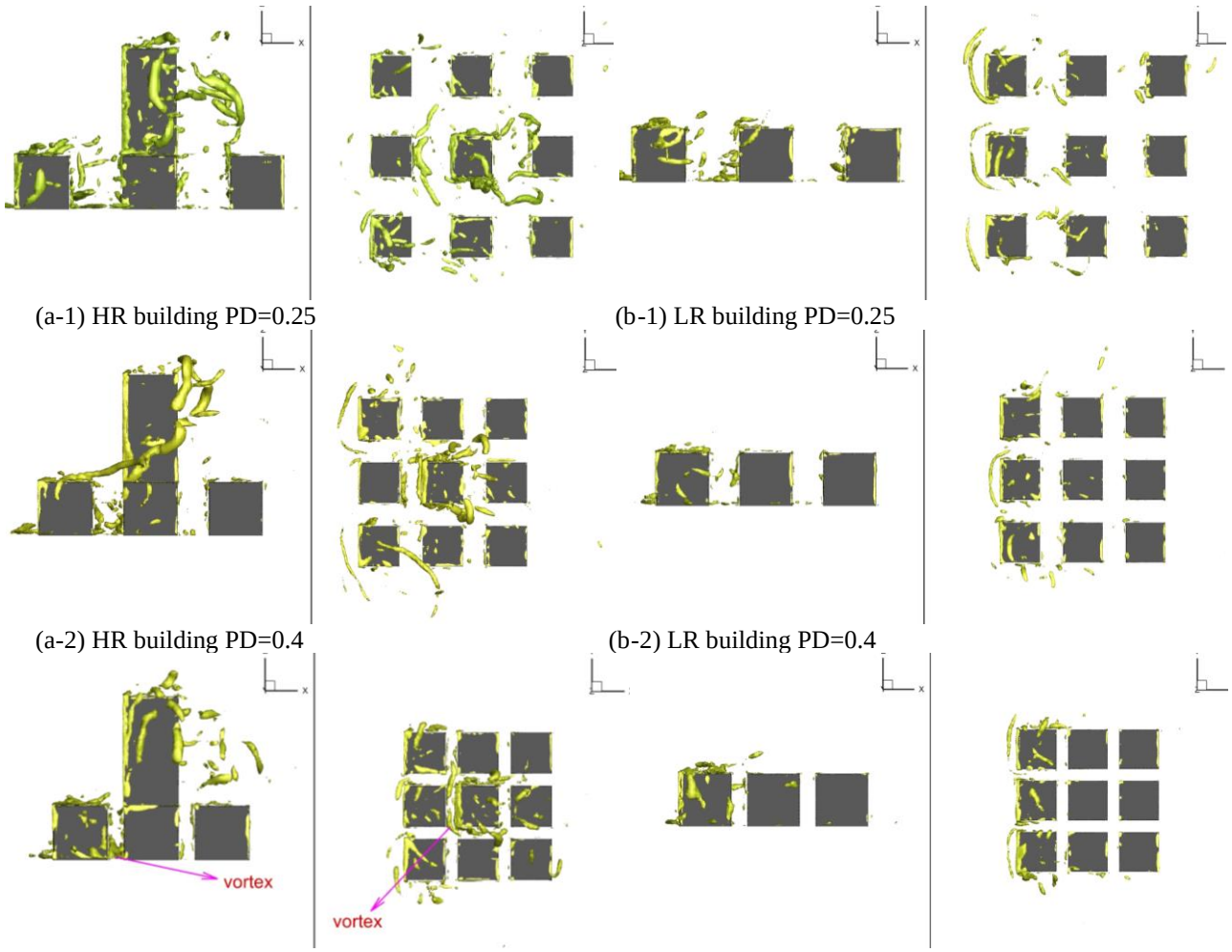

(a-1) HR building PD=0.25 (b-1) LR building PD=0.25

(a-2) HR building PD=0.4 (b-2) LR building PD=0.4

(a-3) HR building PD=0.6 (b-3) LR building PD=0.6

Fig. 9 Q-criteria=30000 for the urban array cases. a: HR building, b: LR building

around the target LR buildings. For the urban array cases with the HR building, the vortices are produced in front of and at the sides of the HR buildings, over the B4 building and leeward of the B1 buildings. And with the increase of the PD, the vortices cover more area of the canyon.

Figure 10 gives the mean velocity contour on the plane y/h=0 for the urban array cases. Firstly, the velocity around the surrounded LR building decreases with the increase of the planar density and is smaller than that around the HR building. Furthermore, Fig. 10(a-1, a-2, a-3) presents that the downward airflow on the windward face of the HR building speeds up resulting from the increase of the planar density. The velocity on the leeward side of the HR building decreases when the planar density increases. This result suggests that less airflow enters the downstream street for the higher planar density.

Figure 11 displays the turbulence kinetic energy (TKE) contour on the plane y/h=0 for the urban array cases. The TKE around the surrounded LR building decreases with the increase of the planar density. Near the front wall, it is larger than that of the HR building. With the increase of the planar density, the TKE behind the HR building diminishes.

The mean streamlines on the plane z/h=0.1 (the pedestrian level) for the urban array cases are shown in Fig. 12. Due to the downward airflow in front of the HR building, there is no vortex in the upstream street, which is shown in Fig. 12(a-1, a-2, a-3). For the surrounded LR building, when the planar density increases, the effect of the downward airflow is weakened. Then the vortices form in the upstream street. In the downstream street, two symmetrical vortices emerge. With increasing planar density, the size of the vortices dwindles.

The time histories of the horizontal velocity in the wake are shown in Fig. 13. The point s/D=2/3, y/h =0, z/h=0.1 is the monitoring point in the wake, where s is the distance between the point and the back wall of the target building and D is the width of the street. When the planar density is 0.4 or 0.6, the wake behind the HR building is asymmetric for a relatively long time, which is displayed in Fig.12(a-2, a-3) and Fig. 14. Figure 14 shows that the wind flows from one side to another side along the downstream street for a certain time, alternating then in the opposite direction. This is a long-periodic alternating-flow. The probability density function of the horizontal velocity in the wake displayed in Fig. 15 also proves that the alternating wake-flow is more common in the wake of the HR building. This situation reveals that a high-speed area forms in the wake of the HR building. Furthermore, the period of the high speed becomes larger with the increase of the planar density. This special character would discomfort the pedestrian.

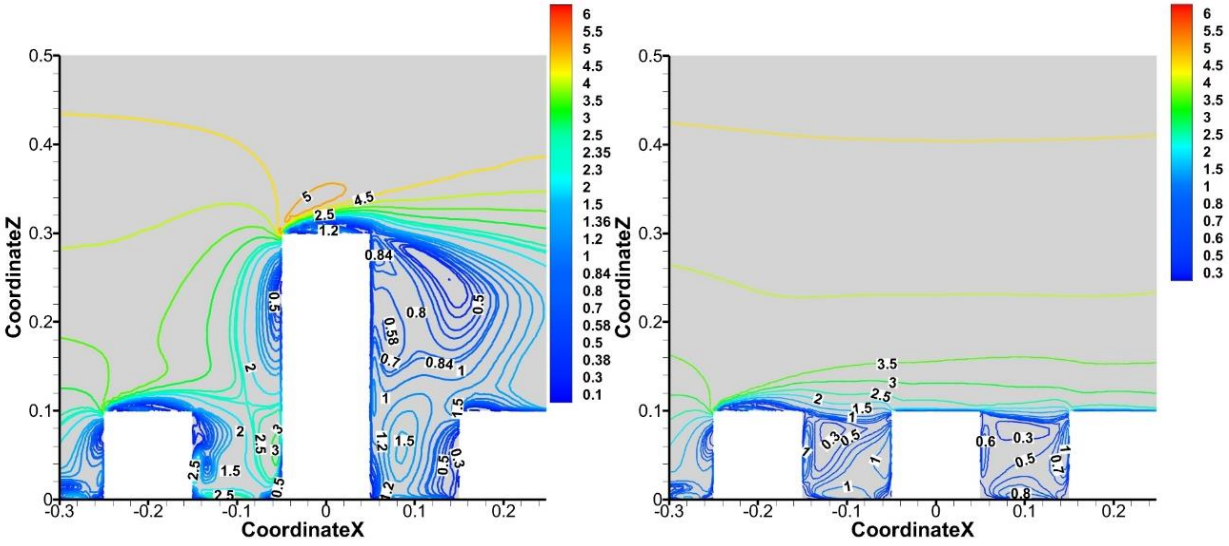

(a-1) HR building PD=0.25 (b-1) LR building PD=0.25

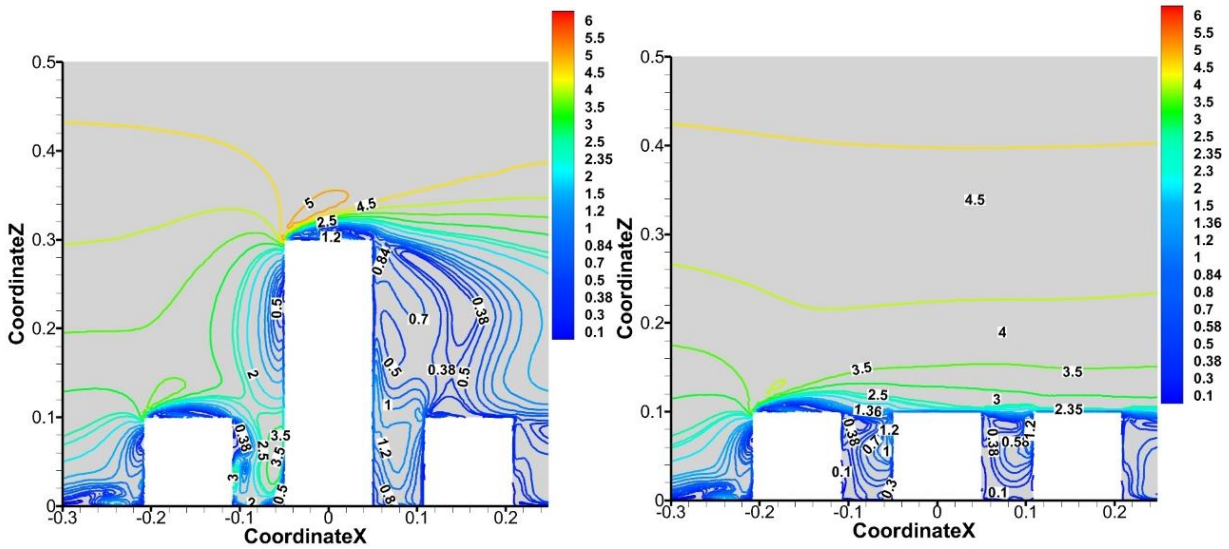

(a-2) HR building PD=0.4 (b-2) LR building PD=0.4

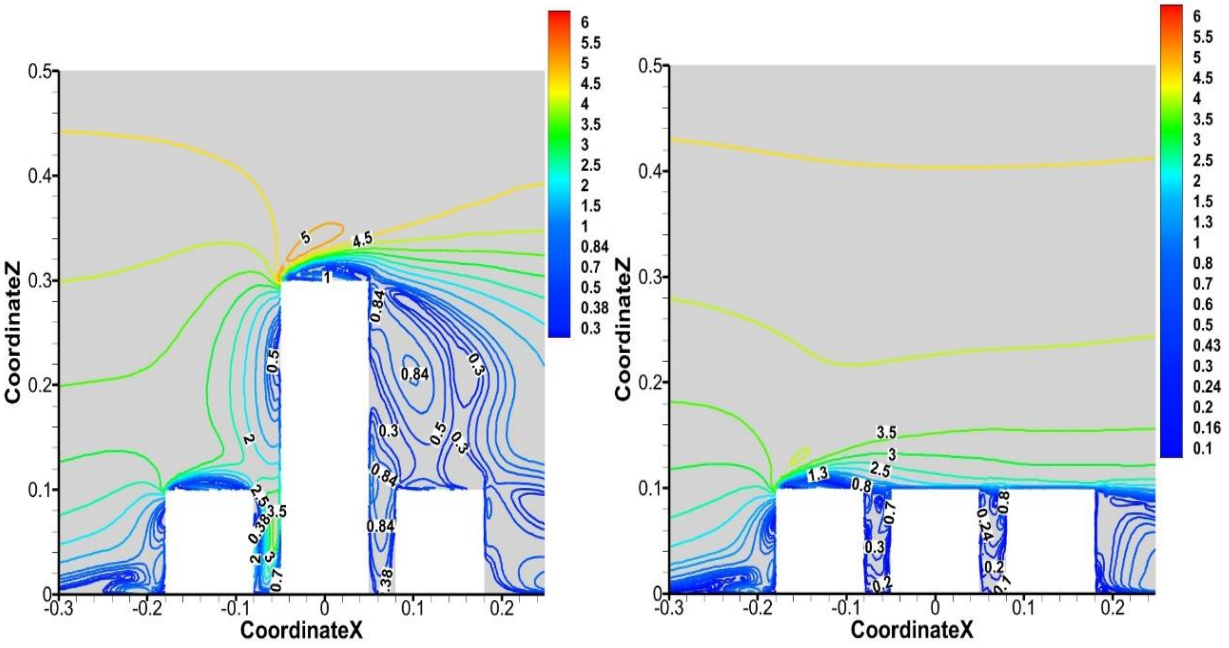

(a-3) HR building PD=0.6 (b-3) LR building PD=0.6

Fig. 10 Mean velocity contour on the plane *y*/*h*=0 for the urban array cases. a: HR building, b: LR building

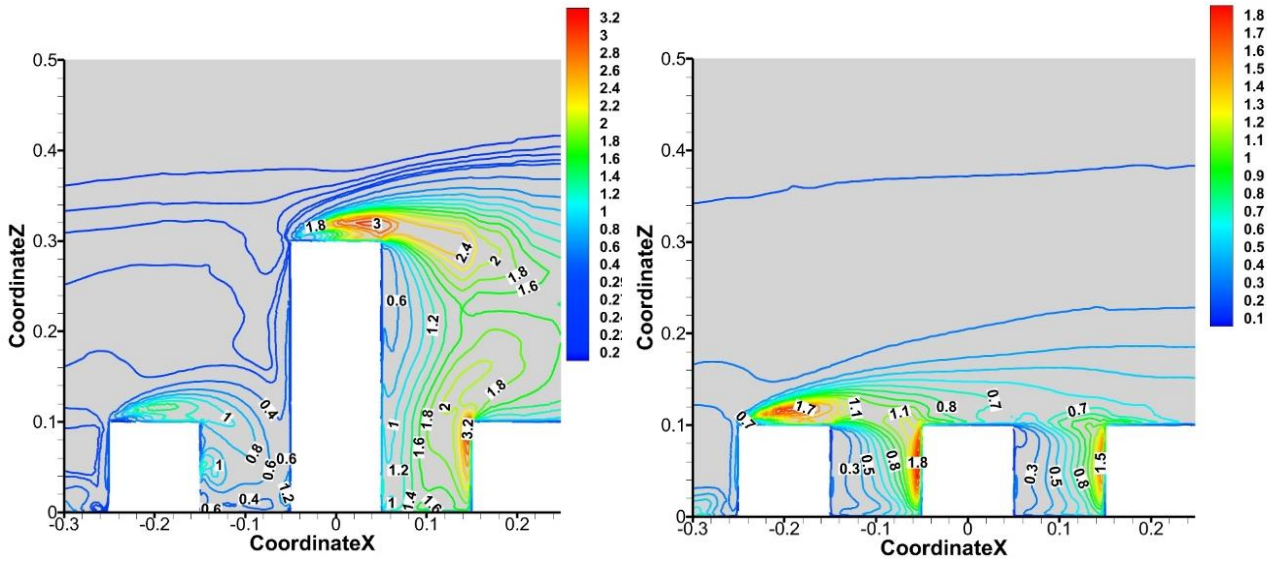

(a-1) HR building PD=0.25 (b-1) LR building PD=0.25

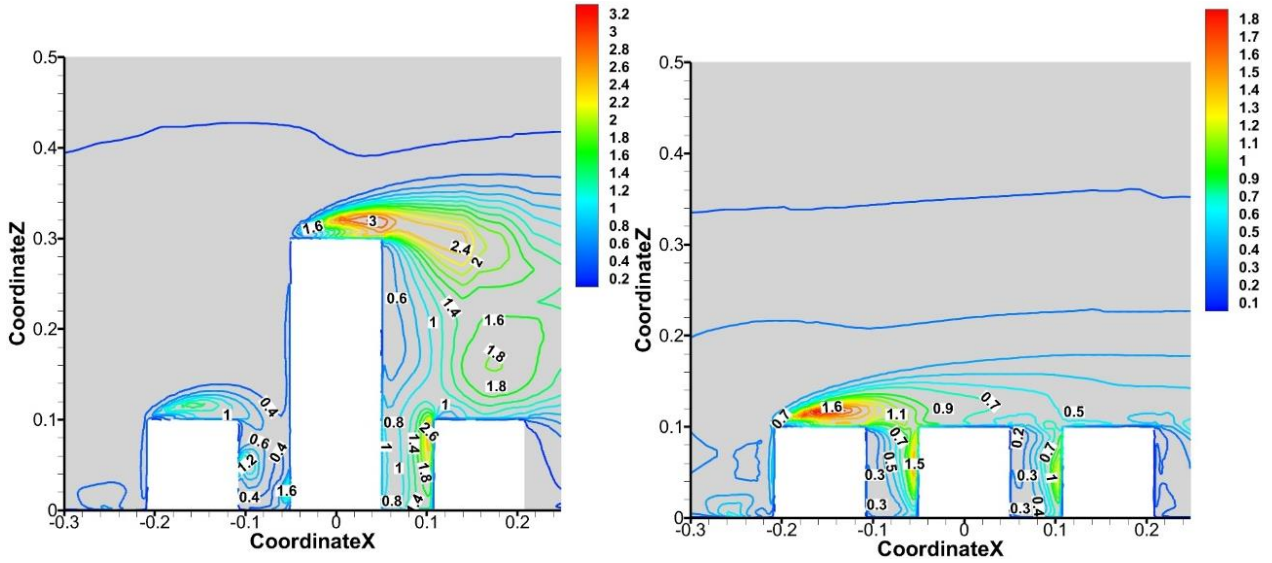

(a-2) HR building PD=0.4 (b-2) LR building PD=0.4

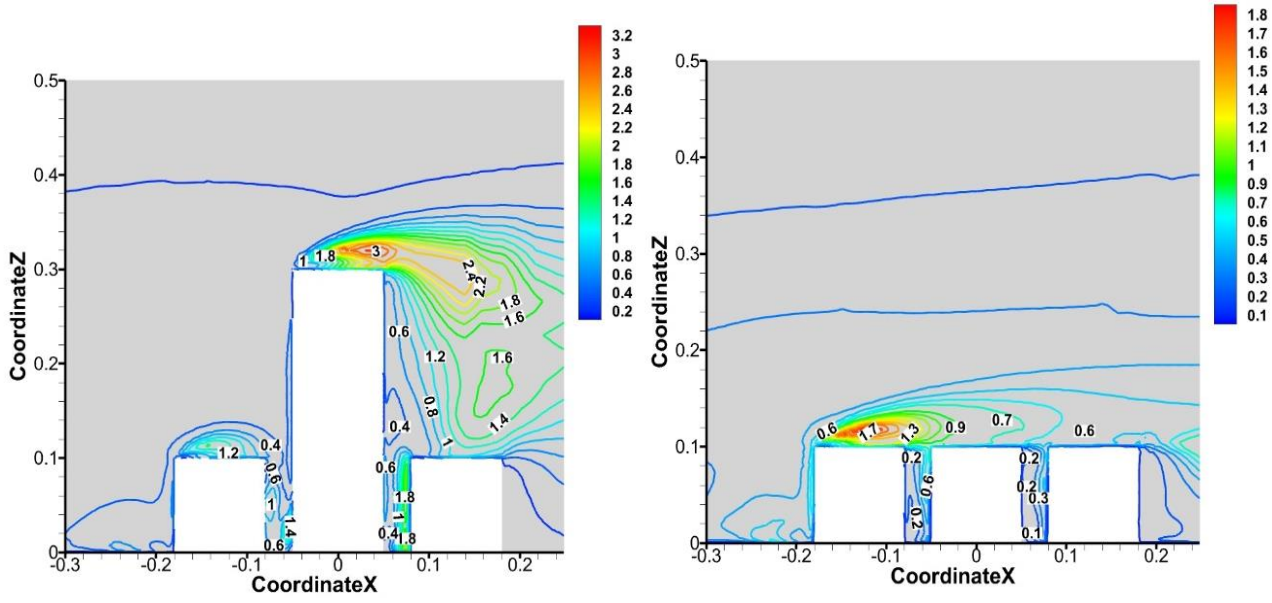

(a-3) HR building PD=0.6 (b-3) LR building PD=0.6

Fig. 11 Turbulence kinetic energy contour on the plane *y*/*h*=0 for the urban array cases. a: HR building, b: LR building

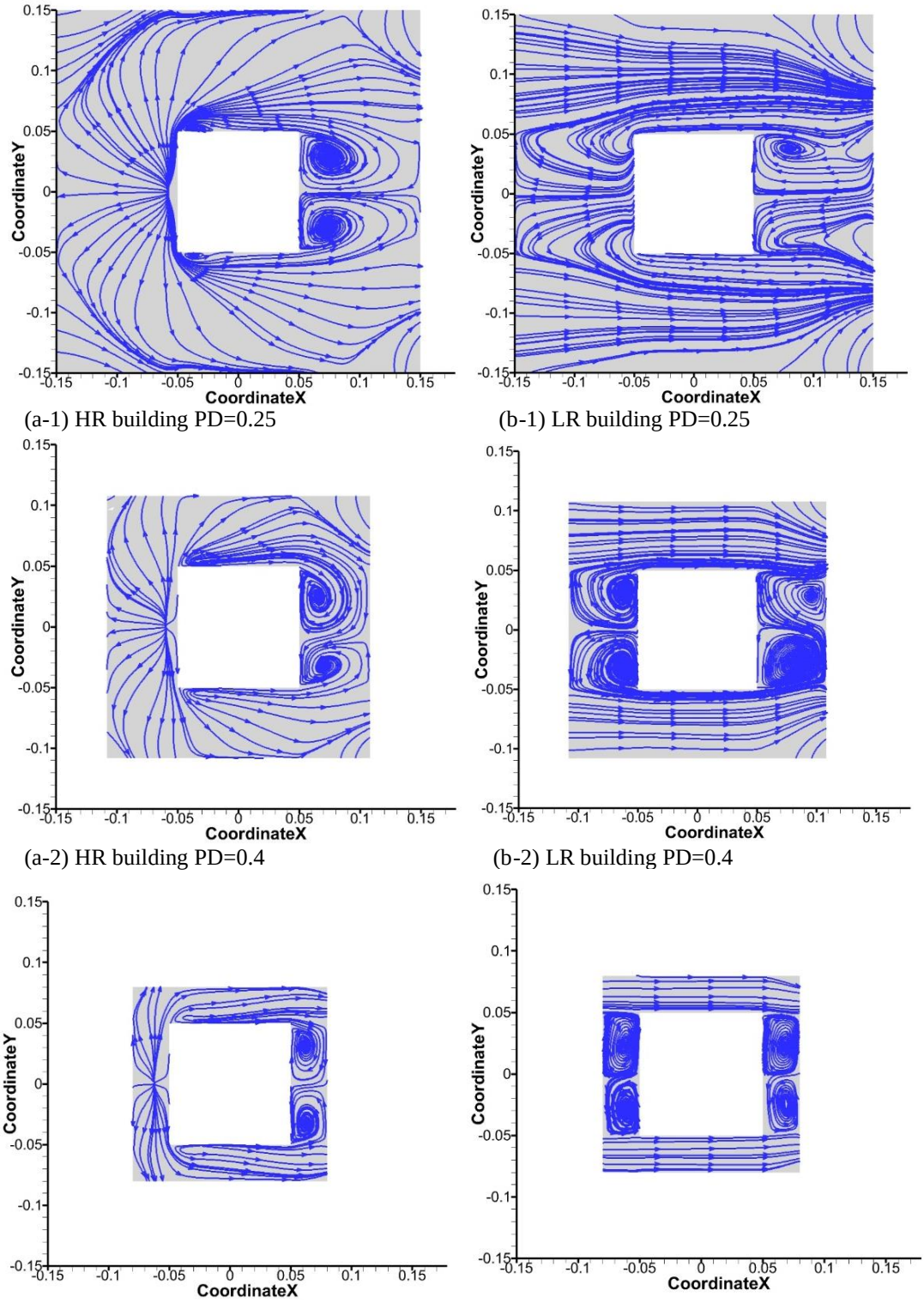

(a-1) HR building PD=0.25 (b-1) LR building PD=0.25

(a-2) HR building PD=0.4 (b-2) LR building PD=0.4

(a-3) HR building PD=0.6 (b-3) LR building PD=0.6

Fig. 12 Mean streamlines on the plane *z*/*h*=0.1 for the urban array cases. a: HR building, b: LR building

The wake asymmetry or the long-period alternating-flow is not a new flow structure. The wake asymmetry appears in the wake of a cylinder with a blockage ratio of 0.7 and 0.9 (Ooi et al., 2022), and two side-by-side cylinders separated by the center-to-center distance T ranging in $1.2<T/D<2.2$ (Sumner, 2010). The asymmetry of the wake is due to the overall confinement of the wake by the channel walls (Ooi et al., 2022). In the urban array cases with an HR building, the asymmetry or the long-periodic alternating-flow in the wake may be a consequence of the close confinement of the side surrounding buildings B2 and B6. While for the LR building array with PD=0.6, there is no alternating-flow. In the windward and the leeward canyons of the LR target building, there is less downward wind. However, lots of downward wind enters the windward and the leeward canyons of the HR target building. This makes more unstable wind environments, leading to the long-periodic alternating-flow.

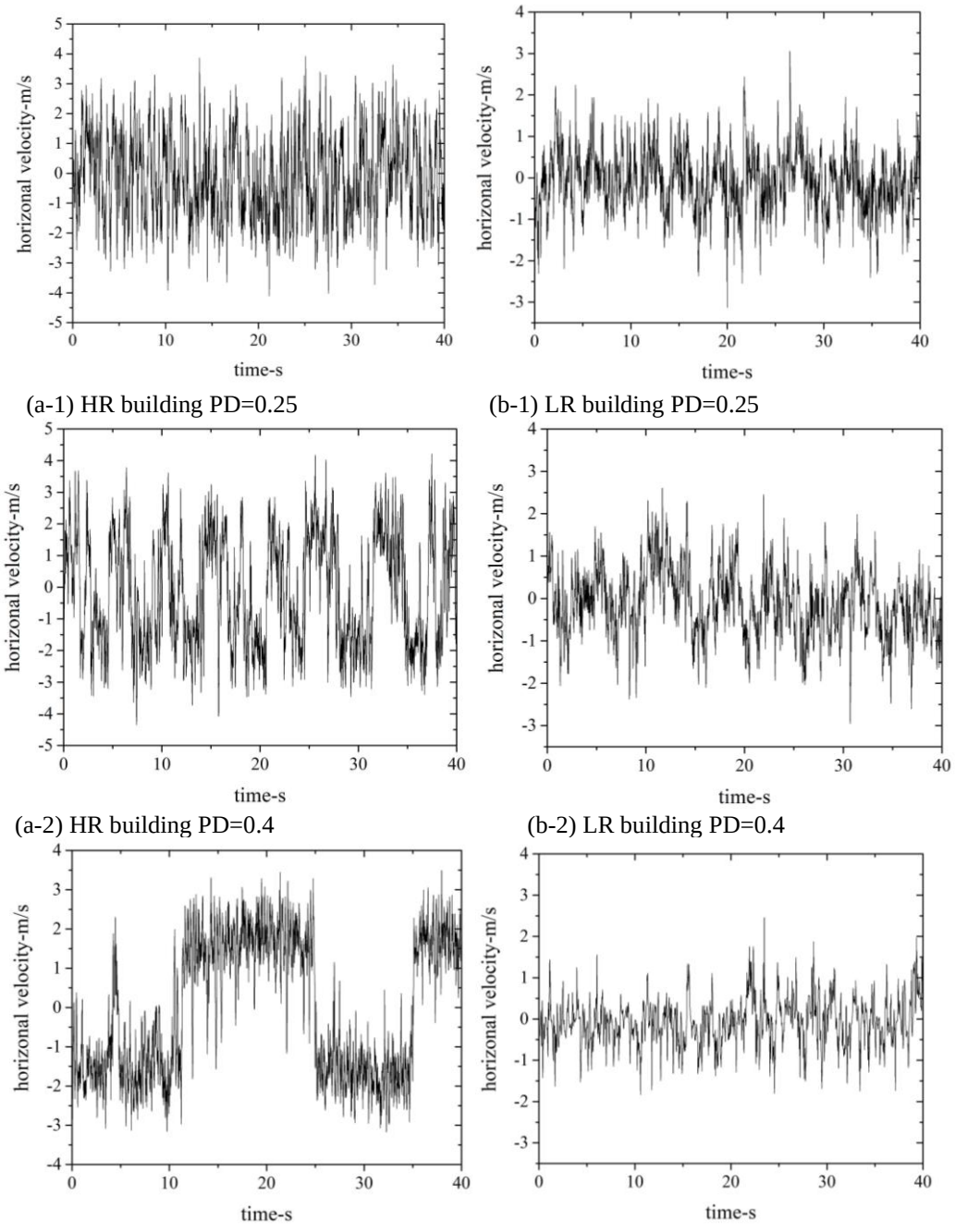

(a-1) HR building PD=0.25 (b-1) LR building PD=0.25

(a-2) HR building PD=0.4 (b-2) LR building PD=0.4

(a-3) HR building PD=0.6 (b-3) LR building PD=0.6

Fig. 13 Time history of the horizontal velocity in the wake. a: HR building, b: LR building

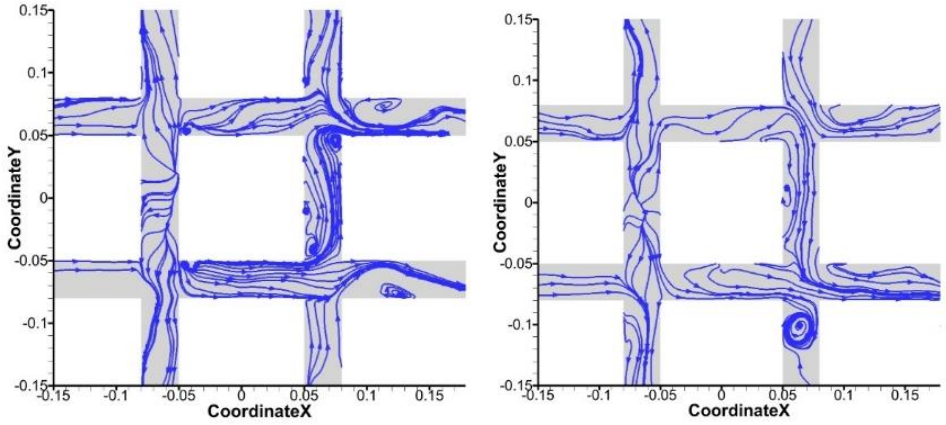

(a) T1 (b) T2

Fig. 14 Instantaneous streamline on the plane *z*/*h*=0.1 around the HR building for the planar density of 0.6

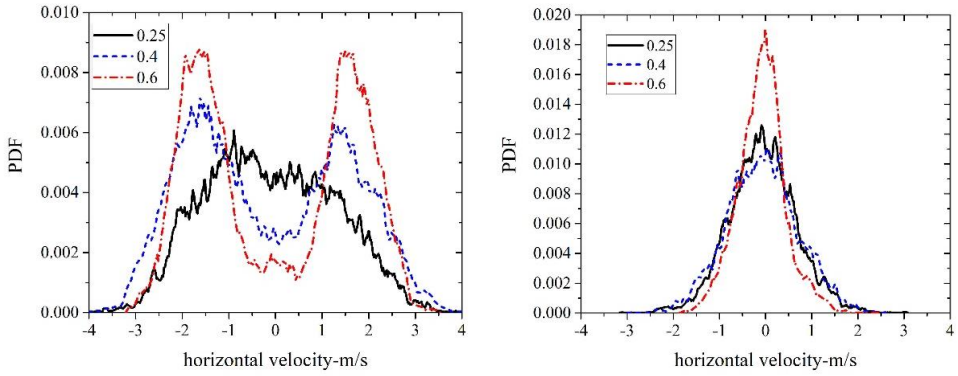

(a) HR building (b) LR building

Fig. 15 Probability density function of the horizontal velocity in the wake

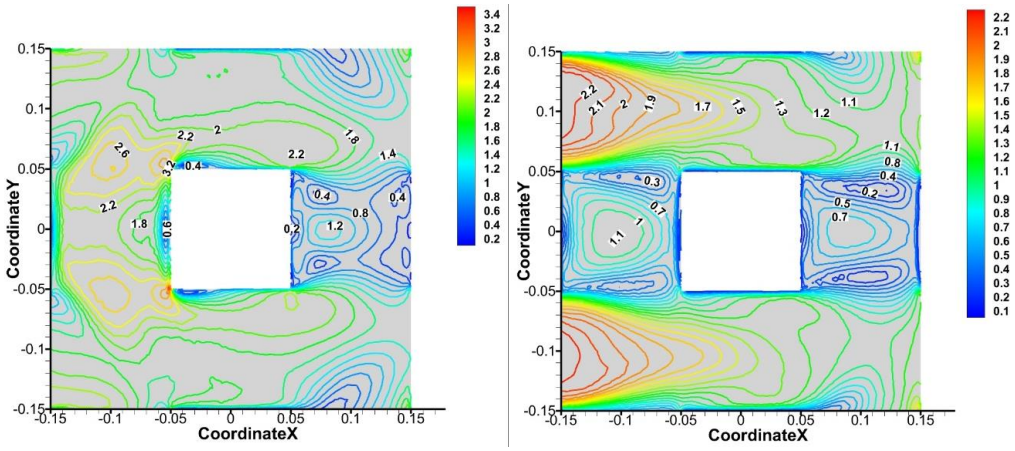

(a-1) HR building PD=0.25 (b-1) LR building PD=0.25

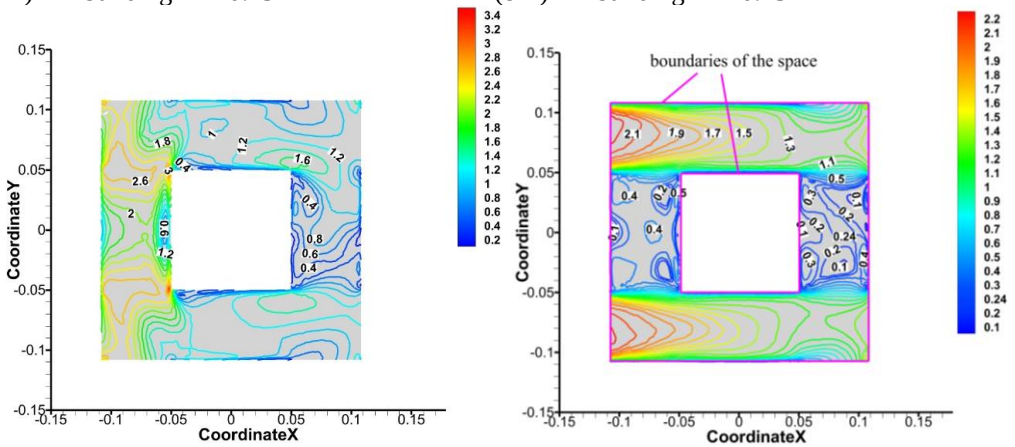

(a-2) HR building PD=0.4 (b-2) LR building PD=0.4

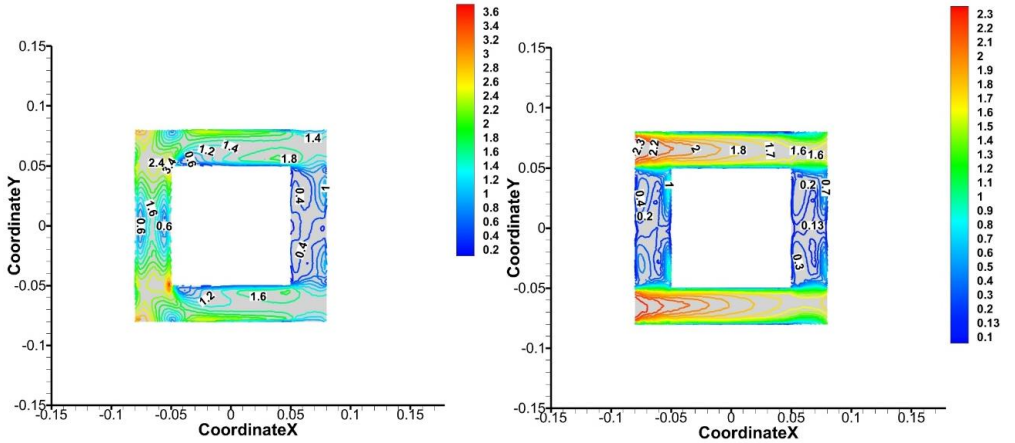

(a-3) HR building PD=0.6 (b-3) LR building PD=0.6

Fig. 16 Mean velocity contour on the plane *z*/*h*=0.1 for the urban array cases. a: HR building, b: LR building

Table 2 Space-averaged mean velocity around the surrounded building at pedestrian level

	Planar density					
	0.25		0.4		0.6	
	V-m/s	V/u_h	V-m/s	V/u_h	V-m/s	V/u_h
LR building	1.137	0.367	1.047	0.338	1.132	0.365
HR building	1.639	0.529	1.371	0.442	1.412	0.455

Table 3 Space-averaged mean temperature around the surrounded building at pedestrian level

	Planar density					
	0.25		0.4		0.6	
	T_{space}	$(T_{space}-T_H)/(T_f-T_H)$	T_{space}	$(T_{space}-T_H)/(T_f-T_H)$	T_{space}	$(T_{space}-T_H)/(T_f-T_H)$
LR building	291.37 K/18.22 ℃	0.20	293.48 K/20.33 ℃	0.27	296.58 K/23.43 ℃	0.36
HR building	289.33 K/16.18 ℃	0.14	290.88 K/17.73 ℃	0.19	292.47 K/19.32 ℃	0.26

Figure 16 gives the mean velocity (time-averaged velocity magnitude) contour on the plane z/h=0.1 (the pedestrian level) for the urban array cases. The space-averaged mean velocity around the surrounded building at pedestrian level is shown in Table 2. The space extends from the wall surfaces of the target building to the nearest surfaces of the nearby buildings B2, B4, B6, B8 on the horizontal plane z/h=0.1 (Fig. 16). This means that the space is the area that is covered by contours in Fig. 16. The velocity around the HR building is larger than that around the surrounded LR building, due to the downward airflow in front of the HR building. For the LR urban array, the velocities in the upstream and the downstream streets drop with increasing planar density. This results from the fact that the narrower upstream and downstream streets hinder the airflow to enter the street. Nevertheless, the velocities in the side streets become larger when the planar density becomes greater. This is due to the stronger "leakage" effect enlarging the speed of the jet airflow. Overall, Table 2 shows that when the planar density increases, the velocity decreases by -7.9%. However, for the planar density of 0.6, the velocity increases by 8.1%.

For the urban array cases with the HR building, the mechanism is different. Table 2 shows that the space-averaged mean velocities around the surrounded HR buildings with a planar density of 0.6 and 0.25 are respectively 19.5% and 3.0% larger than that with a planar density of 0.4. Fig. 16(a-1, b-1, c-1) shows that faster airflow forms near the front surface for the denser array. In the side street, the velocity becomes smaller, then becomes larger with the increase of the planar density. Fig. 12(a-1, b-1, c-1) shows that the airflow in the side street is from the upstream and the downwash airflow for the planar density of 0.25, while the airflows for the planar density of 0.4 and 0.6 are only from the downwash airflows. Because of the absence of the upstream airflow, the velocity in the side street reduces for the planar density of 0.4. When the planar density is 0.6, the narrower side streets lead to a larger velocity. What is more, there is relatively fast air flowing through the downstream street, enlarging the velocity in the downstream street for the sparsest array.

Figure 17 gives the turbulence kinetic energy contour on the plane z/h=0.1 (the pedestrian level) for the urban array cases. Due to the HR building, the TKE around it is enlarged in comparison with the LR surrounded building. Taking attention to the upstream corner of the surrounded buildings, the TKE around the HR building is larger than that around the LR building. This is due to the turbulence produced by the airflow separation at the upstream corner of the HR building, which is presented in Fig. 12(a-1, a-2, a-3). While Fig. 12(b-1, b-2, b-3) show that there is no separation for the LR building.

4.3 Thermal Field

The mean temperature contour on the plane y/h=0 for the urban array cases is shown in Fig. 18. For the LR urban array, the mean temperature increases with increasing the planar density, which is presented in Fig.18 (b-1, b-2, b-3). In comparison with the LR urban array, the temperature around the HR building is lower. This is because of the downwash airflow forming around the HR building removing the heat. When the planar density increases, the temperature in front of the HR building has not a great difference. While, behind the HR and the LR surrounded buildings, the temperatures rise.

Figure 19 gives the mean temperature contour on the plane z/h=0.1 (the pedestrian level) for the urban array cases. The space-averaged mean temperature around the surrounded building at the pedestrian level is shown in Table 3. The temperature around the HR building is lower than that around the surrounded LR building which is shown in Fig. 19 and Table 3, due to the greater velocity. The mean temperature around the surrounded LR building at the pedestrian level increases with the increase of the planar density.

The space-averaged mean temperature around the surrounded HR building increases with the planar density increasing. But the extent of the increase is smaller compared to the LR building. The average increase rates are respectively 9.6% and 13.4% for the HR and the LR buildings. In the upstream street, the temperatures are almost the same in the different urban densities. This is

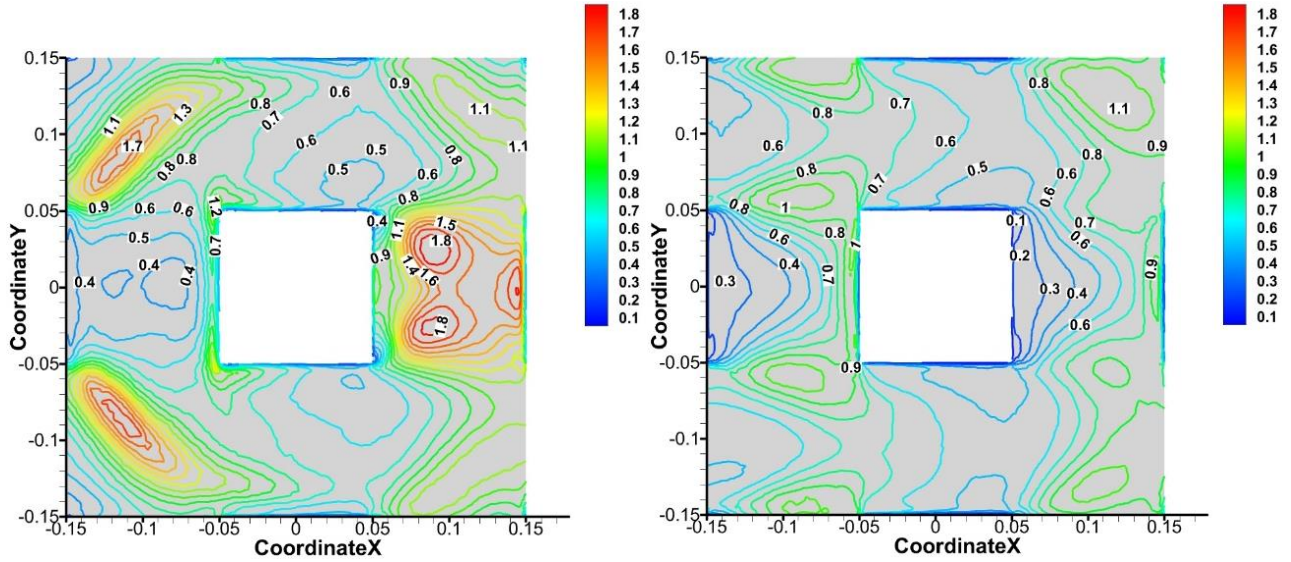

(a-1) HR building PD=0.25 (b-1) LR building PD=0.25

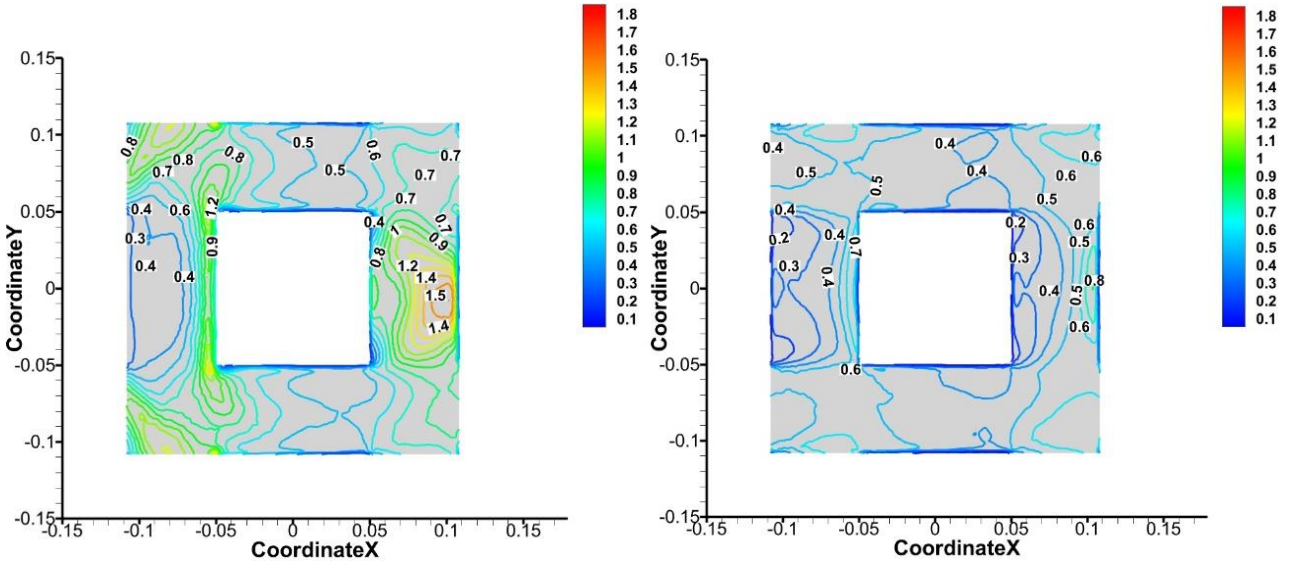

(a-2) HR building PD=0.4 (b-2) LR building PD=0.4

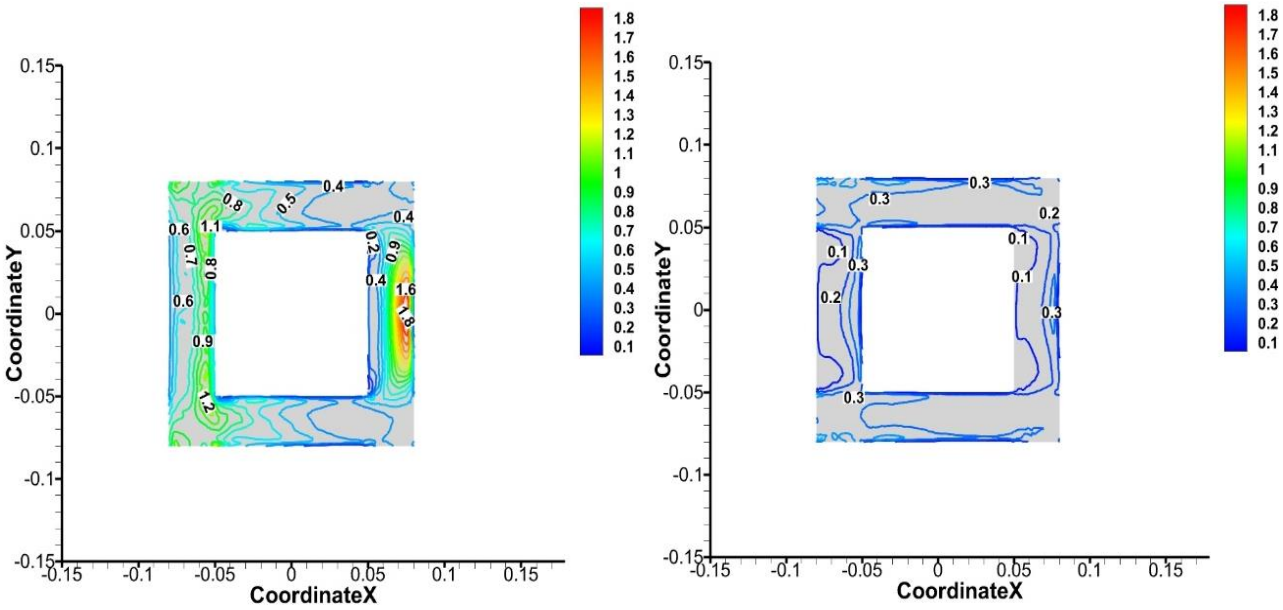

(a-3) HR building PD=0.6 (b-3) LR building PD=0.6

Fig. 17 Turbulence kinetic energy contour on the plane *z*/*h*=0.1 for the urban array cases. a: HR building, b: LR building

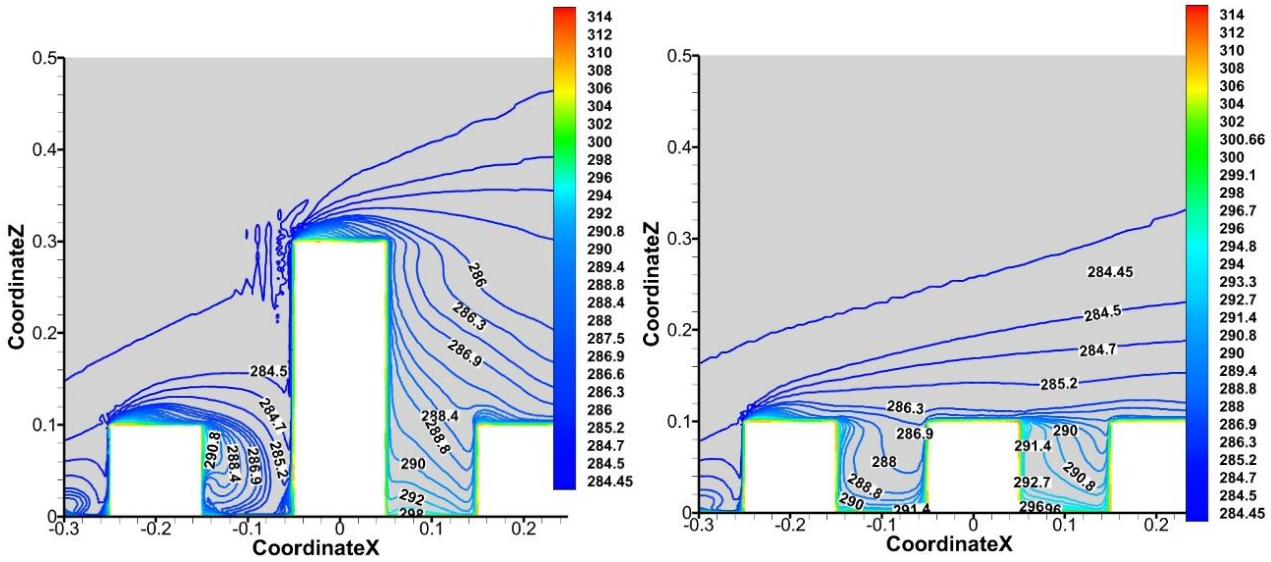

(a-1) HR building PD=0.25 (b-1) LR building PD=0.25

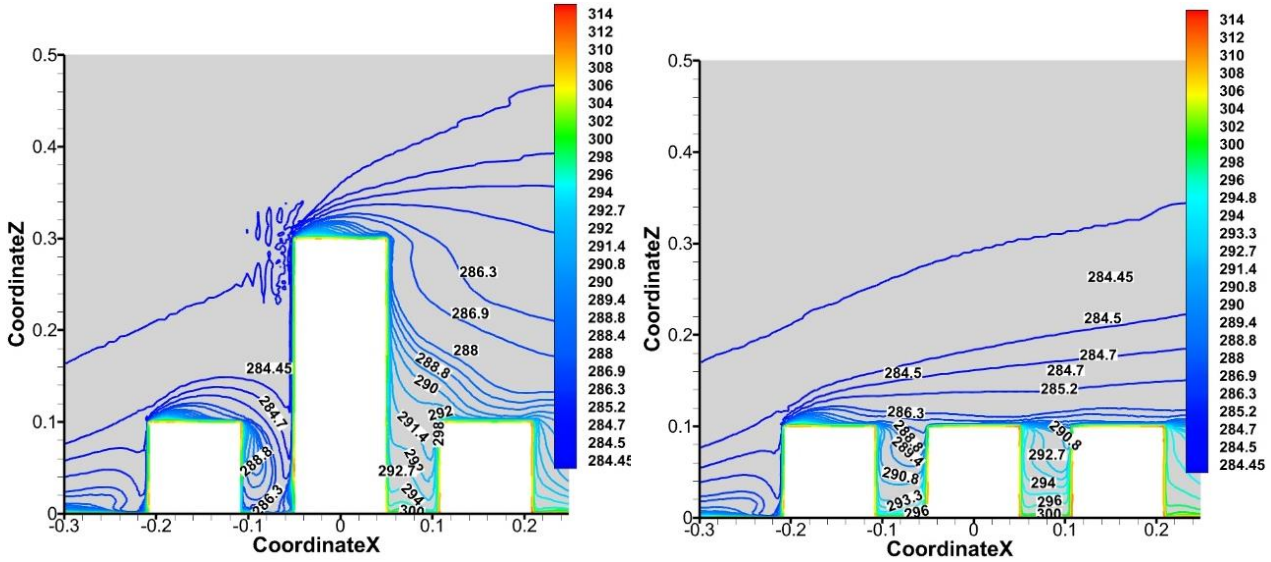

(a-2) HR building PD=0.4 (b-2) LR building PD=0.4

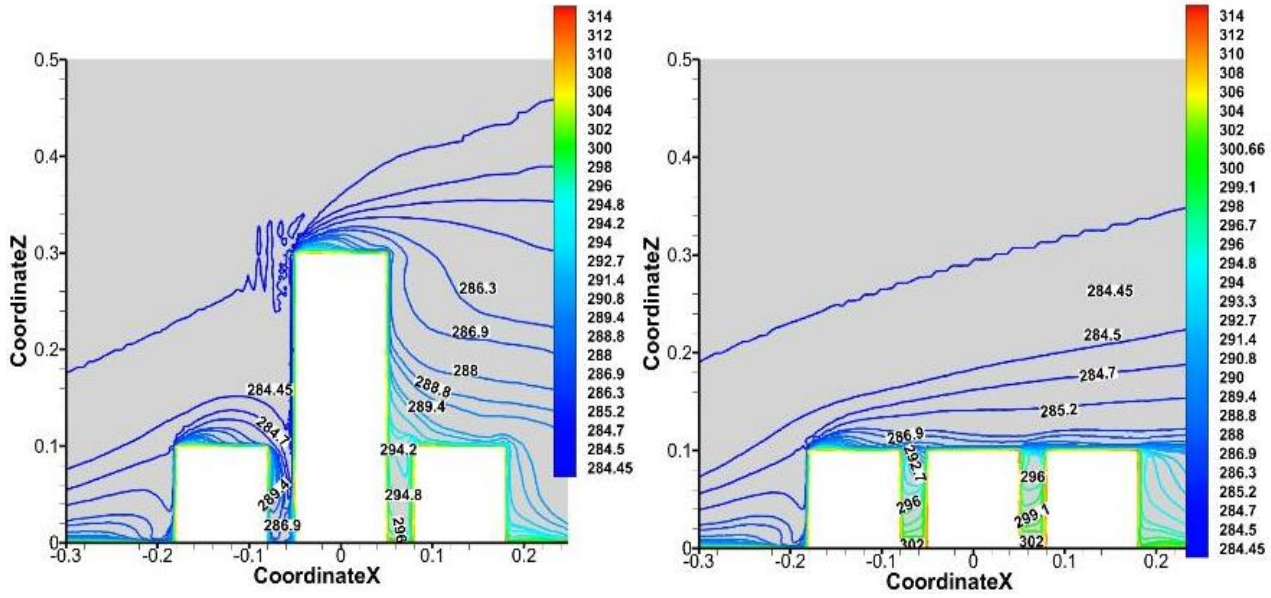

(a-3) HR building PD=0.6 (b-3) LR building PD=0.6

Fig. 18 Mean temperature contour on the plane *y*/*h*=0 for the urban array cases. a: HR building, b: LR building

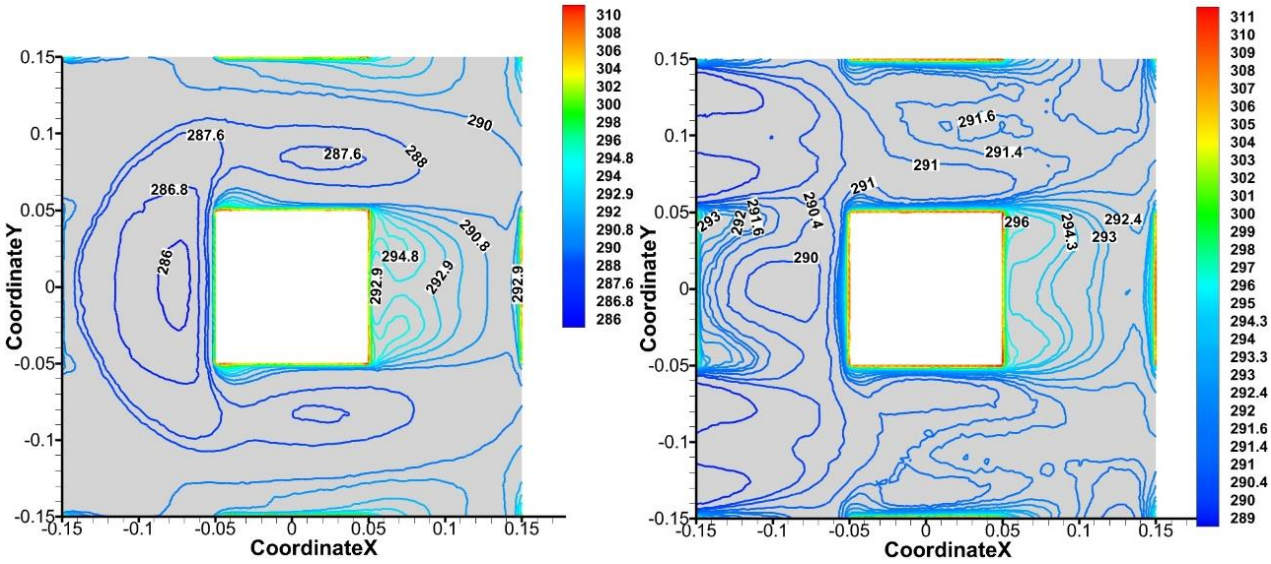

(a-1) HR building PD=0.25 (b-1) LR building PD=0.25

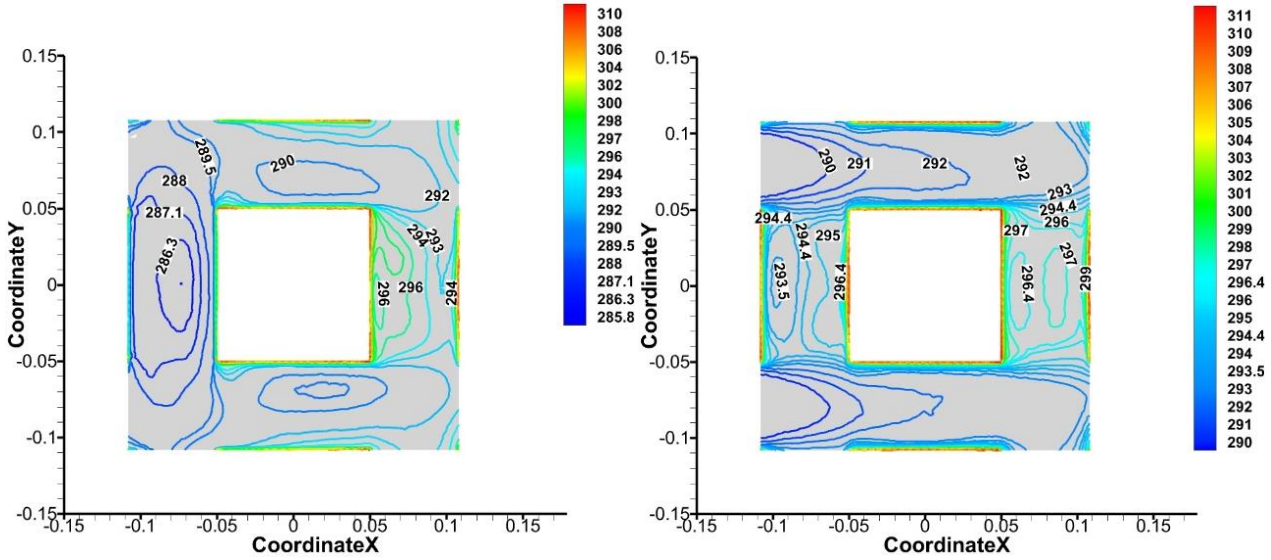

(a-2) HR building PD=0.4 (b-2) LR building PD=0.4

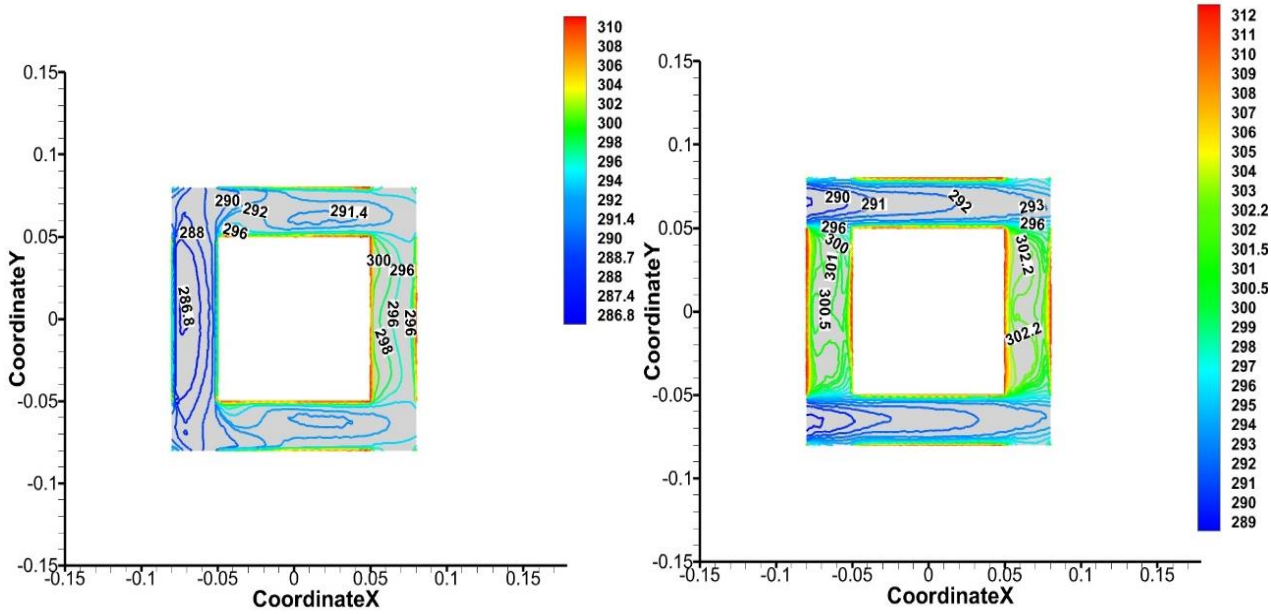

(a-3) HR building PD=0.6 (b-3) LR building PD=0.6

Fig. 19 Mean temperature contour on the plane *z*/*h*=0.1 for the urban array cases. a: HR building, b: LR building

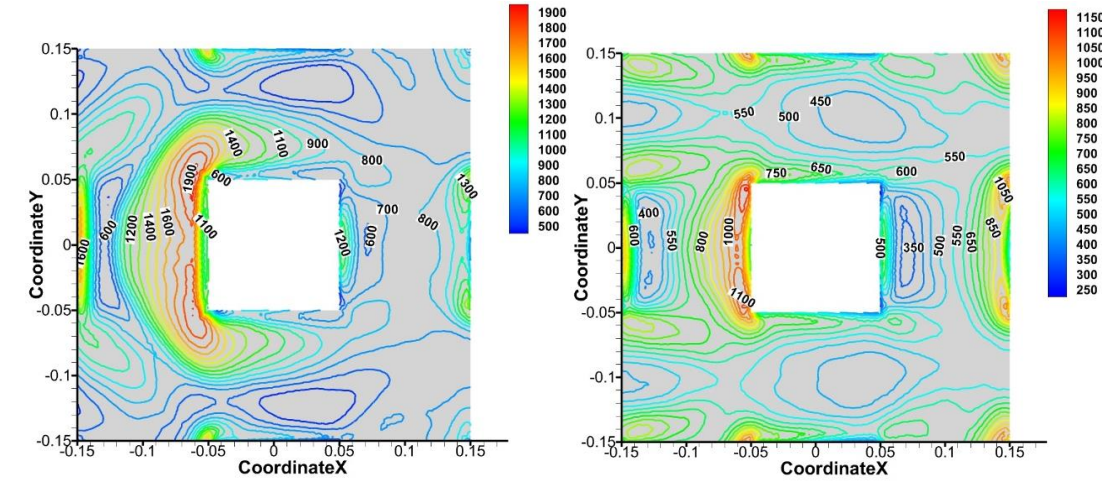

(a-1) HR building PD=0.25 (b-1) LR building PD=0.25

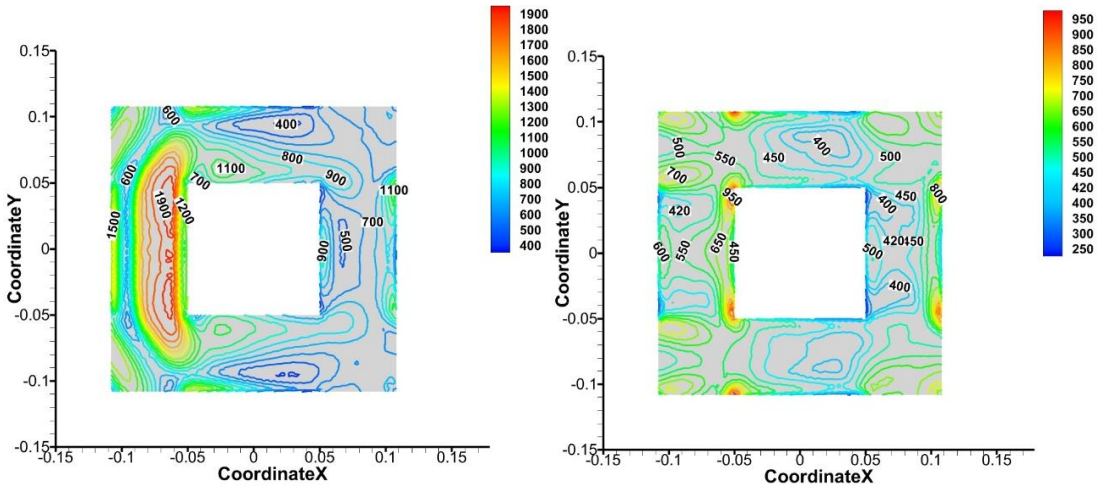

(a-2) HR building PD=0.4 (b-2) LR building PD=0.4

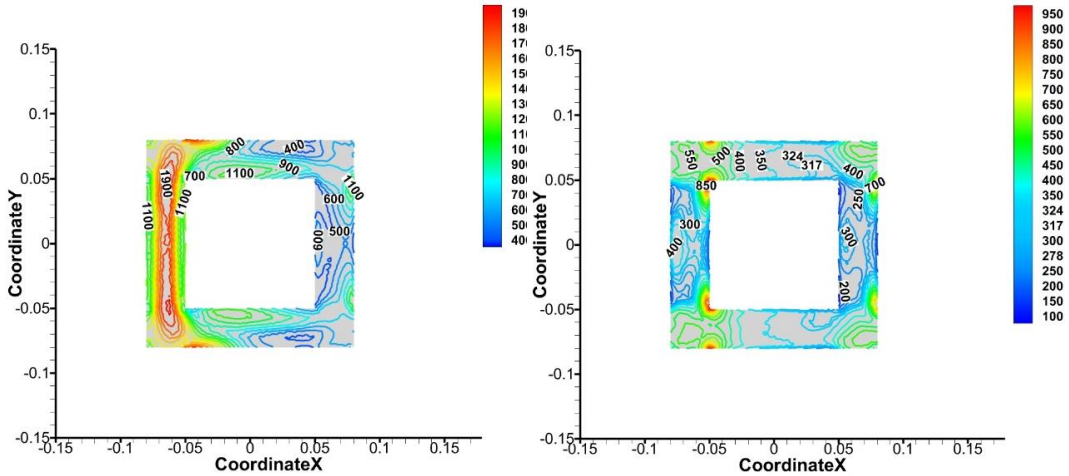

(a-3) HR building PD=0.6 (b-3) LR building PD=0.6

Fig. 20 Mean heat flux contour on the ground surface for the urban array cases. a: HR building, b: LR building

Table 4 Space-averaged mean heat flux on the ground surface for the urban array cases

	Planar density		
	0.25	0.4	0.6
LR building	602.33 W/m^2	520.10 W/m^2	389.26 W/m^2
HR building	867.65 W/m^2	918.51 W/m^2	966.36 W/m^2

because the downwash airflow ventilates the upstream street. When the planar density increases from 0.25 to 0.4, the street becomes narrower. The wind speed weakens in the downstream street, resulting in reduced the heat transfer. Then, the temperature in the downwind street becomes larger, which is shown in Fig. 19(a-1, a-2, a-3). Combining these reasons, the temperature around the surrounded HR building in the dense urban array is greater than these in the moderate urban arrays.

Figure 20 gives the mean heat flux contour on the ground surface for the urban array cases. The mean heat flux around the surrounded LR building decreases at higher planar densities. This is due to the less airflow entering the street for the narrower street. The mean heat flux around the HR building is greater than that around the surrounded LR building, which is given in Table 4. Table 4 is the space-averaged mean heat flux on the ground surface. The space is from the surfaces of the surrounded building to the nearest surfaces of the nearby buildings on the ground surface. Above the ground of the upstream street upwind of the HR building, due to the downwash airflow with low temperature, the forced convection and the temperature gradient are enlarged over there. Then, the heat flux is much larger than that before the surrounded LR building, which is shown in Fig. 20. In the side street and downstream street canyons there is greater speed airflow, leading to a larger heat flux around the HR building.

Table 4 shows that the mean heat flux on the ground surface around the HR building becomes greater at higher planar densities. This is different from the LR array. Fig. 20(a-1, a-2, a-3) displays that the high heat flux area covers a larger region of the upstream and the side streets for the denser array. In the side and the downstream streets, the heat fluxes become smaller with the increase of the planar density, which is led by the velocity of the airflow. Because of the high heat flux covering a larger region with the increase of the planar density, the space-averaged heat flux increases.

5. CONCLUSIONS

The effect of a single high-rise (HR) building on the wind and the thermal environments within the urban array considering different planar densities was studied numerically. The planar densities are 0.25, 0.4 and 0.6. The simulation results reveal that the HR building can affect the flow dynamics and heat transfer mechanisms within the urban array strongly. The conclusions are:

(1) Compared with the low-rise (LR) buildings, the presence of a HR building in building arrays creates high-speed downwash airflow in the upstream street, and this downwash air leads to an increase of the wind speed at pedestrian level. The velocity of downwash airflow increases with increased plane density.

(2) The velocity around the HR building at the pedestrian level first decreases and then increases with the increasing planar density. Compared with LR buildings, due to the existence of downwash airflow, the turbulent kinetic energy at the pedestrian level around the HR building increases, and the fluctuation of the airflow is stronger.

(3) Compared with the wake airflow of the LR target building, when the planar density is large, the wake airflow of the HR building is alternating. And long periods of high-speed airflow occur, which has a significant impact on pedestrian comfort.

(4) The temperature around the HR building is lower than that around the LR building. The time-averaged temperatures at pedestrian level around LR and HR buildings increase with planar density. But the temperature around the high building increases at a slower rate than those around the LR building.

(5) The averaged surface heat flux around the HR building is greater than that around the LR building. The averaged surface heat flux around the HR building increases with the increase of the plane density, which is contrary to that around the LR building.

ACKNOWLEDGEMENTS

This work is supported by the National Natural Science Foundation of China (Grant No. 52078146). We also acknowledge the Network Center of Guangzhou University for providing HPC computing resources.

CONFLICT OF INTEREST

We have no conflicts to disclose.

AUTHORS CONTRIBUTION

P. Ding: Conceptualization; Methodology; Validation; Formal analysis; Writing - Original Draft; Writing - Review & Editing. **X. Zhou**：Funding acquisition；Supervision；Writing - Review & Editing.

REFERENCES

Bazdidi-Tehrani, F., Gholamalipour, P., Kiamansouri, M., & Jadidi, M. (2019). Large eddy simulation of thermal stratification effect on convective and turbulent diffusion fluxes concerning gaseous pollutant dispersion around a high-rise model building. *Journal of Building Performance Simulation*, *12*(1), 97-116. https://doi.org/10.1080/19401493.2018.1486886

Blocken, B., Stathopoulos, T., & Van Beeck, J. (2016). Pedestrian-level wind conditions around buildings: Review of wind-tunnel and CFD techniques and their accuracy for wind comfort assessment. *Building and Environment*, *100*, 50-81. https://doi.org/10.1016/j.buildenv.2016.02.004

Ding, P., & Zhou, X. (2022). A DDES Model with Subgrid-scale Eddy Viscosity for Turbulent Flow. *Journal of Applied Fluid Mechanics*, *15*(3), 831-842. https://doi.org/10.47176/JAFM.15.03.33238

Ding, P., Zhou, X., Wu, H., & Chen, Q. (2022). An efficient numerical approach for simulating airflows around an isolated building. *Building and Environment*, *210*, 108709. https://doi.org/10.1016/j.buildenv.2021.108709

Du, Y., Mak, C. M., & Li, Y. (2019). A multi-stage optimization of pedestrian level wind environment and thermal comfort with lift-up design in ideal urban canyons. *Sustainable Cities and Society*, *46*, 101424. https://doi.org/10.1016/j.scs.2019.101424

Duan, G., & Ngan, K. (2019). Sensitivity of turbulent flow

around a 3-D building array to urban boundary-layer stability. *Journal of Wind Engineering and Industrial Aerodynamics*, *193*, 103958. https://doi.org/10.1016/j.jweia.2019.103958

Duan, G., & Ngan, K. (2020). Influence of thermal stability on the ventilation of a 3-D building array. *Building and Environment*, *183*, 106969. https://doi.org/10.1016/j.buildenv.2020.106969

Gousseau, P., Blocken, B., & Van Heijst, G. J. F. (2013). Quality assessment of large-eddy simulation of wind flow around a high-rise building: Validation and solution verification. *Computers & Fluids*, *79*, 120-133. https://doi.org/10.1016/j.compfluid.2013.03.006

Iqbal, Q. M. Z., & Chan, A. L. S. (2016). Pedestrian level wind environment assessment around group of high-rise cross-shaped buildings: Effect of building shape, separation and orientation. *Building and Environment*, *101*, 45-63. https://doi.org/10.1016/j.buildenv.2016.02.015

Kuo, C. Y., Tzeng, C. T., Ho, M. C., & Lai, C. M. (2015). Wind tunnel studies of a pedestrian-level wind environment in a street canyon between a high-rise building with a podium and low-level attached houses. *Energies*, *8*(10), 10942-10957. https://doi.org/10.3390/en81010942

Lin, Y., Ichinose, T., Yamao, Y., & Mouri, H. (2020). Wind velocity and temperature fields under different surface heating conditions in a street canyon in wind tunnel experiments. *Building and Environment*, *168*, 106500. https://doi.org/10.1016/j.buildenv.2019.106500

Marucci, D., & Carpentieri, M. (2020). Dispersion in an array of buildings in stable and convective atmospheric conditions. *Atmospheric Environment*, *222*, 117100. https://doi.org/10.1016/j.atmosenv.2019.117100

Mathey, F., Cokljat, D., Bertoglio, J. P., & Sergent, E. (2006). Assessment of the vortex method for large eddy simulation inlet conditions. *Progress in Computational Fluid Dynamics, An International Journal*, *6*(1-3), 58-67. https://doi.org/10.1504/PCFD.2006.009483

Menter, F. R. (1994). Two-equation eddy-viscosity turbulence models for engineering applications. *AIAA Journal*, *32*(8), 1598-1605. https://doi.org/10.2514/3.12149

Mittal, H., Sharma, A., & Gairola, A. (2018). A review on the study of urban wind at the pedestrian level around buildings. *Journal of Building Engineering*, *18*, 154-163. https://doi.org/10.1016/j.jobe.2018.03.006

Mittal, H., Sharma, A., & Gairola, A. (2019). Numerical simulation of pedestrian level wind flow around buildings: Effect of corner modification and orientation. *Journal of Building Engineering*, *22*, 314-326. https://doi.org/10.1016/j.jobe.2018.12.014

Nicoud, F., & Ducros, F. (1999). Subgrid-scale stress modelling based on the square of the velocity gradient tensor. *Flow, turbulence and Combustion*, *62*(3), 183-200. https://doi.org/10.1023/A:1009995426001

Ooi, A., Lu, W., Chan, L., Cao, Y., Leontini, J., & Skvortsov, A. (2022). Turbulent flow over a cylinder confined in a channel at Re= 3,900. *International Journal of Heat and Fluid Flow*, *96*, 108982. https://doi.org/10.1016/j.ijheatfluidflow.2022.108982

Shirzadi, M., & Tominaga, Y. (2021). Multi-fidelity shape optimization methodology for pedestrian-level wind environment. *Building and Environment*, *204*, 108076. https://doi.org/10.1016/j.buildenv.2021.108076

Spalart, P. R. (2009). Detached-eddy simulation. *Annual review of Fluid Mechanics*, *41*(1), 181-202. https://doi.org/10.1146/annurev.fluid.010908.165130

Stathopoulos, T. (1985). Wind environmental conditions around tall buildings with chamfered corners. *Journal of Wind Engineering and Industrial Aerodynamics*, *21*(1), 71-87. https://doi.org/10.1016/0167-6105(85)90034-0

Sumner, D. (2010). Two circular cylinders in cross-flow: a review. *Journal of Fluids and Structures*, *26*(6), 849-899. https://doi.org/10.1016/j.jfluidstructs.2010.07.001

Tamura, Y., Xu, X., Tanaka, H., Kim, Y. C., Yoshida, A., & Yang, Q. (2017). Aerodynamic and pedestrian-level wind characteristics of super-tall buildings with various configurations. *Procedia Engineering*, *199*, 28-37. https://doi.org/10.1016/j.proeng.2017.09.146

Tamura, Y., Xu, X., & Yang, Q. (2019). Characteristics of pedestrian-level Mean wind speed around square buildings: Effects of height, width, size and approaching flow profile. *Journal of Wind Engineering and Industrial Aerodynamics*, *192*, 74-87. https://doi.org/10.1016/j.jweia.2019.06.017

Tominaga, Y., & Shirzadi, M. (2021). Wind tunnel measurement of three-dimensional turbulent flow structures around a building group: Impact of high-rise buildings on pedestrian wind environment. *Building and Environment*, *206*, 108389. https://doi.org/10.1016/j.buildenv.2021.108389

Tsang, C. W., Kwok, K. C. S., & Hitchcock, P. A. (2012). Wind tunnel study of pedestrian level wind environment around tall buildings: Effects of building dimensions, separation and podium. *Building and Environment*, *49*, 167-181.

Tse, K.-T., Zhang, X., Weerasuriya, A. U., Li, S. W., Kwok, K. C. S., Mak, C. M., & Niu, J. (2017). Adopting 'lift-up'building design to improve the surrounding pedestrian-level wind environment. *Building and Environment*, *117*, 154-165. https://doi.org/10.1016/j.buildenv.2017.03.011

Uematsu, Y., Yamada, M., Higashiyama, H., & Orimo, T.

(1992). Effects of the corner shape of high-rise buildings on the pedestrian-level wind environment with consideration for mean and fluctuating wind speeds. *Journal of Wind Engineering and Industrial Aerodynamics*, *44*(1-3), 2289-2300. https://doi.org/10.1016/0167-6105(92)90019-7

Van Druenen, T., Van Hooff, T., Montazeri, H., & Blocken, B. (2019). CFD evaluation of building geometry modifications to reduce pedestrian-level wind speed. *Building and Environment*, *163*, 106293. https://doi.org/10.1016/j.buildenv.2019.106293

Xia, Q., Liu, X., Niu, J., & Kwok, K. C. S. (2017). Effects of building lift-up design on the wind environment for pedestrians. *Indoor and built Environment*, *26*(9), 1214-1231. https://doi.org/10.1177/1420326X15609967

Yoshie, R. (2016). *Wind tunnel experiment and large eddy simulation of pollutant/thermal dispersion in non-isothermal turbulent boundary layer.* Advanced Environmental Wind Engineering, Springer.

Zhang, X., Tse, K. T., Weerasuriya, A. U., Li, S. W., Kwok, K. C. S., Mak, C. M., Lin, Z. (2017). Evaluation of pedestrian wind comfort near 'lift-up'buildings with different aspect ratios and central core modifications. *Building and Environment*, *124*, 245-257. https://doi.org/10.1016/j.buildenv.2017.08.012